

# The Phoenix Survey: Optical and Near-Infrared Observations of Faint Radio Sources

A. Georgakakis<sup>1,2</sup>, B. Mobasher<sup>2</sup>, L. Cram<sup>3</sup>, A. Hopkins<sup>3</sup>, C. Lidman<sup>4</sup>,  
M. Rowan-Robinson<sup>2</sup>

<sup>1</sup> *School of Physics and Astronomy, University of Birmingham, Edgbaston, B15 2TT, UK*

<sup>2</sup> *Astrophysics Group, Blackett Laboratory, Imperial College, Prince Consort Rd, London SW7 2BZ, UK*

<sup>3</sup> *Astrophysics Department, School of Physics, University of Sydney, NSW, Australia 2006*

<sup>4</sup> *European Southern Observatory, Casilla 19001, Santiago 19, Chile*

13 October 2018

## ABSTRACT

Using a deep Australia Telescope Compact Array (ATCA) radio survey covering an area of  $\approx 3 \text{ deg}^2$  to a  $4\sigma$  sensitivity of  $\geq 100 \mu\text{Jy}$  at 1.4 GHz, we study the nature of faint radio galaxies. About 50% of the detected radio sources are identified with an optical counterpart revealed by CCD photometry to  $m_R=22.5$  mag. Near-infrared ( $K$ -band) data are also available for a selected sample of the radio sources, while spectroscopic observations have been carried out for about 40% of the optically identified sample. These provide redshifts and information on the stellar content. Emission-line ratios imply that most of the emission line sources are star-forming galaxies, with a small contribution ( $\approx 10\%$ ) from Sy1/Sy2 type objects. We also find a significant number of absorption line systems, likely to be ellipticals. These dominate at high flux densities ( $>1 \text{ mJy}$ ) but are also found at sub-mJy levels. Using the Balmer decrement we find a visual extinction  $A_V=1.0$  for the star-forming faint radio sources. This moderate reddening is consistent with the  $V - R$  and  $R - K$  colours of the optically identified sources. For emission line galaxies, there is a correlation between the radio power and the  $H\alpha$  luminosity, in agreement with the result of Benn *et al.* (1993). This suggests that the radio emission of starburst radio galaxies is a good indicator of star-formation activity.

**Key words:** Galaxies: active – galaxies: starburst – Cosmology: observations – radio continuum: galaxies

## 1 INTRODUCTION

Deep radio surveys (Windhorst *et al.* 1985; Windhorst *et al.* 1993; Fomalont *et al.* 1997; Hopkins *et al.* 1998) have revealed a flattening in the normalized source counts below  $S_{1.4} \approx 10 \text{ mJy}$  suggesting the emergence of a new population of faint radio sources. Photometric (Thuan *et al.* 1984, 1992; Kron *et al.* 1985; Windhorst *et al.* 1985; Thuan & Condon 1987) and spectroscopic studies (Benn *et al.* 1993) reveal that the sources responsible for the flattening are predominantly star-forming galaxies, similar to those of the IRAS starburst population. The proportion of active galactic nuclei (AGNs) is much smaller than it is at higher flux densities (Benn *et al.* 1993; Gruppioni *et al.* 1998; Kron *et al.* 1985). However, the local density of star-forming radio sources is too small to explain the turn-up point and slope of the  $\log N / \log S$  curve. Moreover, evolutionary models of the radio sources that dominate the counts at high flux densities

cannot reproduce these features either (Danese *et al.* 1987; Danese, De Zotti & Franceschini 1985). Therefore, models for the source counts invoke strong evolution of either spiral galaxies (Condon 1989; Dunlop & Peacock 1990), or star-forming IRAS population galaxies (Danese *et al.* 1987; Rowan-Robinson *et al.* 1993; Hopkins *et al.* 1998).

Visual inspection of faint radio sources shows that many have optical counterparts which are preferentially located in pairs or small groups exhibiting disturbed optical morphologies, suggestive of interactions or mergers (Kron *et al.* 1985; Gruppioni *et al.* 1998). Although this method is not an ideal way to identify physically associated groups, the frequency of cases suggests that such phenomena are partially responsible for the enhanced star formation rate seen in these objects (Kron *et al.* 1985; Windhorst *et al.* 1995).

Further evidence for the appearance of a new population at faint radio flux densities comes from measurements

of angular sizes. These show that at flux densities below a few mJy, the median angular size drops abruptly to few arcseconds (Coleman & Condon 1985; Oort *et al.* 1987). This can be reconciled if faint radio sources are associated with spiral galaxies with radio morphology more compact than that of ellipticals which dominate at higher flux densities (Coleman & Condon 1985).

Despite the effort devoted to the study of the faint radio population there is still no clear answer to the following questions: (i) what is the stellar population in sub-mJy radio sources and how do they evolve with redshift, (ii) what is their relation to the local population of normal galaxies and (iii) how are the star-formation activity and radio properties of these objects related. To address these points we present a deep and homogeneous radio (1.4 GHz) survey (Phoenix), covering an area of  $3 \text{ deg}^2$  combined with optical ( $V$ ,  $R$ -band) and near infrared ( $K$ -band) photometry and optical spectroscopy.

The observations, astrometric calibration, catalogue generation and optical identifications are described in section 2. The final catalogue is presented in section 3, while the data analysis and the results are discussed in section 4. Finally, section 5 summarises our conclusions. Throughout this paper we assume a value  $H_0 = 50 \text{ km s}^{-1} \text{ Mpc}^{-1}$  and  $q_0 = 0.5$ .

## 2 OBSERVATIONS

### 2.1 Radio Observations

The radio observations were made at 1.46 GHz using the 6A configuration of the Australia Telescope Compact Array (ATCA). The mosaic of 30 pointing centres covers a  $2^\circ$  diameter area centered at  $\text{RA}(2000) = 01^{\text{h}} 14^{\text{m}} 12^{\text{s}}.16$ ;  $\text{Dec.}(2000) = -45^\circ 44' 8''.0$  (galactic latitude  $b = -71^\circ$ ). This field, hereafter referred to as the Phoenix Deep Field (PDF), is shown as the large disk in Figure 1. Additional observations were made with a single pointing centered at  $\text{RA}(2000) = 01^{\text{h}} 11^{\text{m}} 13^{\text{s}}.0$ ;  $\text{Dec.}(2000) = -45^\circ 45' 0''.0$ . This is referred to as the Phoenix Deep Field Sub-region (PDFS), covering 36 arcmin diameter and shown in Figure 1 as the small disk. The synthesised beam FWHM for the PDFS and for each of the PDF pointing centres is  $\approx 6$  and  $\approx 8$  arcsec respectively.

Details of the observations, image formation, source extraction and catalogue generation are presented in Hopkins *et al.* (1998). In summary, a source is included into the catalogue if its peak flux density is  $4\sigma$  above the local RMS and if it is confirmed by visual inspection. A total of 938 sources with fluxes  $S_{1.4} > 0.2 \text{ mJy}$  are detected within the PDF and 232 sources are extracted from the 36 arcmin diameter area of the PDFS, to the limiting flux of  $0.1 \text{ mJy}$ . The combined radio catalogue consists of 1079 individual sources identified on both fields. There are two kinds of incompleteness in the catalogue, as with any sample limited by peak flux density. The first is a loss of sensitivity due to the attenuation of the primary beam away from a field center. This has been minimized in the Phoenix survey by the mosaicing strategy used. The second is the fact that extended objects with a total flux density above the survey limit can be missed by an algorithm which initially detects candidates based on

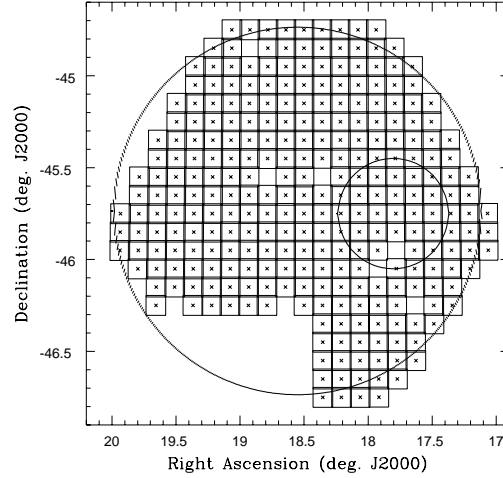


**Figure 1.** The area covered by the Phoenix Deep Field (large disk) and the Phoenix Deep Field Subregion (small disk). Individual CCD  $R$ -band frames are depicted as squares with a cross in the middle

their peak flux densities. Methods of correcting these effects have been described by Hopkins *et al.* (1998). The PDF catalogue is  $\approx 80\%$  complete to  $0.4 \text{ mJy}$ , while the PDFS is  $\approx 90\%$  complete to  $0.15 \text{ mJy}$ .

### 2.2 Optical Photometric Observations

#### 2.2.1 Observations and data reduction

Optical CCD photometry of the Phoenix Field was carried out at the Anglo-Australian Telescope (AAT) during two observing runs in 1994, 1995 September, in the  $V$  and  $R$ -bands. In both runs, the TEK 1K CCD camera was mounted at the  $f/3.3$  prime focus, giving an image scale of  $0.39'' \text{ pixel}^{-1}$  and a field of view of  $6.5' \times 6.5'$ . The exposure time was 120 and 60 sec for the  $V$  and  $R$ -band observations respectively. Between successive pointings the telescope was offset by  $6'$  in right ascension or declination. About 85% areal coverage was achieved in the  $R$ -band (Fig. 1). However, due to poor weather conditions, only half of the Phoenix field has yet been surveyed in the  $V$ -band.

The optical data were reduced following standard procedures, using IRAF tasks. Firstly, the optical CCD frames were debiased using the overscan strip. Secondly, dome-flats were employed to flat-field the images. Bad pixel columns were removed by interpolating between adjacent columns. Photometric calibration was performed using standard stars from Landolt (1992). These provide both the instrumental zero point and the atmospheric extinction relation due to airmass. The photometric accuracy, estimated using these standard stars, is better than  $\approx 0.01 \text{ mag}$  for both  $V$  and  $R$ -band observations.

### 2.2.2 Catalogue Construction

The sources in the reduced optical frames were extracted using the FOCAS package (Jarvis & Tyson 1981). The main input parameters are the detection threshold, given as a multiple of the sky variance ( $\sigma_{Sky}$ ) and the minimum area in pixels for an object to be extracted. After considerable experimentation, we adopted a threshold of  $2.5 \times \sigma_{Sky}$  and a minimum area of 25 pixels ( $\approx 4 \text{ arcsec}^2$ ). This choice of values minimises the number of spurious detections, while ensuring that most faint galaxies are successfully extracted. For each individual frame we masked out vignetted corners and regions contaminated by bright stars, to avoid obviously spurious detections. The catalogues generated for each individual frame were then merged into a final catalogue. Because of the overlap between adjacent frames, a number of objects are recorded more than once. These records are replaced by a single object in the catalogue. A final visual inspection removed any remaining spurious detections. The completeness limit of the  $R$ -band catalogue is found to be  $\approx 22.5 \text{ mag}$  (Appendix A).

### 2.2.3 Astrometry

The astrometry on the optical images is carried out using the APM catalogue to locate  $\approx 10$  stars on each frame. Using the STARLINK ASTROM software, an astrometric model relating the pixel positions of those stars to their astrometric positions was calculated for each frame. The astrometric coordinates of all the objects on that frame were then determined. To estimate the accuracy of the astrometry, the positions of overlapping sources on the APM plates and on our CCD frames were compared. They were found to have an RMS of  $\approx 0.7''$ .

### 2.2.4 Optical identification of the radio sources

To identify optically the sources detected in the radio survey we used the  $R$ -band observations, which are deeper than the  $V$ -band data and have the more complete areal coverage. We followed the technique employed by Downes *et al.* (1986), calculating the probability that a given candidate is the identification by using Bayes' theorem: Consider an optically detected candidate with magnitude  $m$  at a distance  $r$  from the radio position. Given the surface density of objects brighter than  $m$ ,  $\Sigma(< m)$ , the expected number of candidates within  $r$  is

$$\mu = \pi r^2 \Sigma(< m). \quad (1)$$

Assuming that source positions are Poissonian, the probability of at least one object brighter than  $m$  within radius  $r$  is

$$P = 1 - \exp(-\mu), \quad (2)$$

which reduces to  $\mu$  for  $\mu \ll 1$ . In this case, the candidate is unlikely to be a chance association. We apply an upper limit in the search radius,  $r < 10''$  and a cutoff in the probability,  $P < 0.05$ , to limit the optical identifications to those candidates that are least likely to be spurious alignments (Hopkins 1998a). The background density of the objects

(both galaxies and stars) is calculated from our  $R$ -band observations to the limiting magnitude of  $m_R = 22.0 \text{ mag}$  (Appendix A). At fainter magnitudes we used the surface density of objects found by Metcalfe *et al.* (1995). As a result, we propose 504 identifications to the limiting magnitude  $m_R = 22.5 \text{ mag}$  for a total of 1079 radio sources ( $\approx 47\%$ ).

### 2.2.5 Optical Photometry

To estimate colours, the flux in the  $V$  and  $R$ -bands is integrated within an effective aperture corresponding to a physical size of  $\approx 15 \text{ kpc}$  radius at the redshift of the galaxy. This choice of aperture ensures that a substantial fraction of the galaxy light is enclosed. This minimizes the effect of colour gradients while increasing the S/N, especially at faint magnitudes where the uncertainties are dominated by the photon statistics of the sky background.

To facilitate comparison with other studies and to recognize that the aperture scheme used to estimate colour will tend to underestimate the fluxes of the brightest and most extended sources we used the 'total' magnitude calculated by FOCAS as an estimate of the total galaxy optical flux. The FOCAS 'total' magnitude is calculated by integrating the luminosity within an aperture defined by adding rings around the object until the detection area is exceeded by a factor of 2.

## 2.3 Near-Infrared imaging

The near-infrared observations used the IRAC2b camera at the 2.2m European Southern Observatory (ESO) telescope at La Silla and CASPIR at the 2.3m Australian National University (ANU) telescope. Because of the small detector format of the infrared arrays, pointed observations of a total of 46 individual radio sources were carried out.

(i) The ESO observations were carried out on 1991 September 24-27 at the Cassegrain focus of the 2.2m telescope. IRAC2b is a  $256 \times 256$  pixel NIMCOS-3 detector with  $0.5'' \text{ pixel}^{-1}$ , giving a field of view of  $2' \times 2'$ . We observed 34 radio sources within the PDFS, having sub-mJy radio flux densities and optical magnitudes in the range  $19.0 < m_R < 22.0$ .

Dithering observations of each source consisted of a sequence of 6 integrations of 10 sec each, or of 4 integrations of 15 sec each, followed by an offset of the telescope. The number of integrations and the exposure time were adjusted to the seeing conditions, to avoid saturation of the array. To get accurate sky frames, the offset vector was changed between successive observations. The total exposure time varied from 15 min to 1 h depending on the optical magnitude of the candidate. The filter used was  $K'$  (Wainscoat and Cowie 1992).

After dark-field subtraction, each image was flat-fielded using dome flats. An illumination correction, accounting for the large scale sensitivity gradients of the array, was also applied (see ESO manual<sup>\*</sup>). The sky frame to be subtracted

\* <http://epu.ls.eso.org/lasilla/Telescopes/2p2T/E2p2M/IRAC2>

from a given target frame was generated by median combining the 20 images closest in time to the frame in question. The sky-subtracted frame was then smoothed using a  $100 \times 100$  pixel median filter, designed to preserve as much as possible the photometric integrity of the data. All the images of the same source were coadded to produce the final image.

Photometric calibration used standards from Carter and Meadows (1995). The zero points in the calibration equations were stable, with a night-to-night variation less than 0.10 mag. The uncertainty in the zero point is estimated to be less than  $\approx 0.02$ .

(ii) The ANU near-infrared observations were carried out on 1997 November 8-10 at the Cassegrain focus of the 2.3m telescope. CASPIR uses a Santa Barbara Research Center CRC463  $256 \times 256$  InSb detector array with a scale of  $0.5'' \text{ pixel}^{-1}$ , giving a field of view of  $2' \times 2'$ . A total of 12 sub-mJy radio sources with optical counterparts brighter than  $m_R = 19.0$  mag were observed. These observations were carried out in non-photometric conditions.

As with the ESO observations, a dithering technique was adopted, consisting of a sequence of 12 integrations of 5 sec each followed by an offset of the telescope. The total exposure time for each target object was 17 min. The filter used was  $K_n^\dagger$  which is somewhat different from  $K'$ . However, the difference between the two bands is relatively small ( $\leq 0.1$  mag) and does not affect any of our conclusions.

The data reduction followed a procedure similar to that described for the ESO observation. Photometric calibration was performed using faint standard stars from Carter and Meadows (1995). A mean extinction relation was derived for all the nights together. Because of the non-photometric conditions, the uncertainty in the estimated zero point in the calibration equation was  $\approx 0.14$  mag. However, both the zero point and the extinction coefficient agree, within the errors, with typical values reported in the CASPIR manual ( $ZP_{K_n} = 20.5$ , extinction =  $0.10 \text{ mag airmass}^{-1}$ ).

## 2.4 Spectroscopic Observations

Spectroscopic data were obtained using slit spectroscopy at the ESO 3.6 m telescope and multi-object fibre spectroscopy at the 2 degree field spectroscopic facility (2dF) at the AAT.

### 2.4.1 Slit Spectroscopy

The spectra of 20 of the 34 candidates observed in  $K'$  were obtained using EFOSCI at the Cassegrain focus of the 3.6m ESO telescope at La Silla, on 1996 October 9-10. Two gratings were used, covering the wavelength ranges  $5940\text{-}9770 \text{ \AA}$  ( $7.5 \text{ \AA pixel}^{-1}$ ) and  $3640\text{-}6860 \text{ \AA}$  ( $6.3 \text{ \AA pixel}^{-1}$ ). The spatial scale of the detector is  $0.61'' \text{ pixel}^{-1}$ . A  $1.5''$  slit on the first night and a  $2.0''$  slit during the second night were used, with an integration time varying from 10 to 30 min depending on the brightness of the object.

Data reduction was carried out using the Starlink FIFARO package. Firstly, the bias frames were co-added and

then subtracted from the target frames. Secondly, dome-flats, produced by a halogen lamp, were employed to flat-field the data. The wavelength calibration was carried out using a helium-argon spectral lamp, while a relative flux calibration was performed using LTT377 spectrophotometric standard (Hamuy *et al.* 1994). Finally, a wavelength dependent correction for extinction was applied. Values for the extinction parameter at La Silla were taken from the ESO observers' manual.

Although the faintest spectra have low S/N, all but one of the target objects were assigned a redshift based on one or more emission lines.

### 2.4.2 2-degree Field Spectroscopy

Multi-fibre spectroscopy was carried out using 2dF at the prime focus of AAT. The 2dF instrument is designed to allow simultaneous acquisition of up to 400 spectra of objects within a  $2^\circ$  diameter field on the sky. It consists of two spectrographs, each having 200 fibres and two  $1024 \times 1024$  thinned Tektronix CCDs each receiving 200 fibres. The fibres are  $\approx 2$  arcsec in diameter resulting in 2 pixel wide spectra on the detectors. The data for the present study were obtained during two observing runs in 1996 December and 1997 September. At the time, only one of the two spectrographs was operating, resulting in a total of 200 spectra per exposure.

The optical candidates selected for the 2dF observation had  $m_R < 21.5$  mag and were segregated into groups according to their optical magnitude. The total exposure time varied from 1.5 h for the brightest objects to 3.5 h for the optically fainter ones (carried out in 3 to 7 half-hour exposures). The grating used was the 270R, having 75% throughput over the wavelength range  $5000 < \lambda < 8500 \text{ \AA}$ , with a dispersion of  $199.9 \text{ \AA mm}^{-1}$ . The spectral resolution was  $\lambda/\Delta\lambda \approx 600$  with a pixel scale of  $\approx 4.7 \text{ \AA pixel}^{-1}$ .

The spectroscopic data reduction was performed using the 2DFDR package, developed for the reduction of 2dF data. No atmospheric extinction correction was applied to the spectra. This was found to be negligible, since most of the observations were carried out at relatively low zenith distances ( $< 40^\circ$ ). Redshifts were determined by visual inspection of the resulting spectra. Each spectroscopically observed source was assigned an index,  $Q$ ,  $0 < Q < 3$ , indicating the quality of the redshift measurement. A value  $Q = 3$  corresponds to three or more identified spectral features, indicating a firmly established redshift. A value  $Q = 0, 1$  and  $2$  corresponds to none (no redshift determination), one and two identified spectral features respectively. Redshifts were established for 221 out of 312 candidate optical identifications observed with 2dF. Since there was an overlap of 12 objects between the sources observed with ESO 3.6 m telescope and those observed using the 2dF, the total number of determined redshifts, from both runs, is 228 out of 320. The redshifts of the common objects in the spectroscopic runs were found to be consistent with an RMS of  $\approx 0.001$ . Furthermore, to measure the strengths of diagnostic emission lines (see section 4.1), a relative flux calibration was performed using a crude response function provided by the 2dF team. This was calculated by estimating the 2dF efficiency in 3 bands (B, V, R) and then interpolating using a second order polynomial.

<sup>†</sup> <http://msowww.anu.edu.au/observing/docs/manual>

Table 1

#	RA (J2000)	Dec (J2000)	$m_V$	$m_R$	$m_K$	$S_{1.4}$ (mJy)	$V - R$	$R - K$	$z$	$Q$	$\log P_{1.4}$ (W/Hz)	$M_R$	$\log L_{H\alpha}$ (W)	$EW_{H\alpha}$ (Å)	$EW_{[O\ III] \ 3727}$ (Å)	class
1	1 8 33.092	-45 45 44.26	20.79	19.98		0.536	$0.87 \pm 0.05$		0.570	1	23.93	-23.09	35.11		$14 \pm 6$	Unclassified
2	1 8 37.132	-45 48 22.15		15.85		0.614			0.027	3	21.29	-20.22	33.84	$25 \pm 1$		Star-forming
3	1 8 53.884	-45 58 39.63	18.91	18.11		1.093	$0.77 \pm 0.02$		0.233	3	23.44	-22.98				Absorption
4	1 9 11.680	-46 2 8.03	18.02	17.55		0.622	$0.50 \pm 0.01$		0.090	3	22.35	-21.17	34.13	$21 \pm 5$		Star-forming
5	1 9 13.254	-45 34 16.30	18.56	17.86		2.394	$0.61 \pm 0.02$		0.147	3	23.37	-21.86	34.38	$20 \pm 4$	$21 \pm 14$	Sy2
6	1 9 13.448	-45 53 23.08	20.92	19.55		3.947	$1.34 \pm 0.07$		0.530	3	24.73	-23.84	34.87		$4 \pm 3$	Unclassified
7	1 9 33.278	-45 48 23.74	19.28	18.64	16.45	0.519	$0.64 \pm 0.02$	$2.14 \pm 0.22$	0.133	3	22.61	-21.03	34.45	$49 \pm 5$	$25 \pm 24$	Unclassified
8	1 9 33.721	-45 31 14.84	21.41	20.24		1.481	$1.31 \pm 0.14$		0.608	2	24.43	-23.84				Absorption
9	1 9 38.970	-45 39 24.31	23.00	21.58		0.291	$0.55 \pm 0.04$		0.421	1	23.39	-20.66	33.96		$9 \pm 4$	Unclassified
10	1 9 46.386	-45 50 2.40	21.36	20.08		1.779	$1.53 \pm 0.09$		0.545	1	24.41	-23.67				Absorption
11	1 9 47.936	-45 51 24.92	15.48	14.96		0.599	$0.56 \pm 0.01$		0.020	3	21.02	-20.44	33.62	$13 \pm 2$		Star-forming
12	1 9 50.075	-45 46 28.41	19.01	18.33		0.419	$0.67 \pm 0.02$		0.301	3	23.25	-23.24	35.09		$12 \pm 6$	Star-forming
13	1 9 56.949	-46 21 58.91	21.46	20.70		0.443	$0.68 \pm 0.06$		0.663	3	23.98	-22.89	35.62		$54 \pm 24$	Star-forming
14	1 9 57.499	-45 34 57.29		19.26	15.66	0.393		$3.62 \pm 0.03$	0.242	3	23.02	-21.86	34.32	$17 \pm 2$	$60 \pm 46$	Unclassified
15	1 10 6.207	-45 21 51.65		20.60		0.600			0.542	3	23.93	-22.77	34.36		$3 \pm 1$	Absorption
16	1 10 9.684	-45 30 59.95		19.02		3.279			0.372	3	24.33	-23.20				Absorption
17	1 10 16.232	-45 47 32.02	20.33	19.53	16.43	0.231	$0.83 \pm 0.04$	$3.17 \pm 0.04$	0.373	3	23.18	-22.56	35.19		$27 \pm 8$	Star-forming
18	1 10 18.180	-45 49 4.41	20.69	20.47		0.333	$0.45 \pm 0.06$		0.258	3	23.01	-20.64	34.45		$29 \pm 17$	Star-forming
19	1 10 23.404	-45 3 37.69		19.70		2.533			0.572	1	24.61	-23.87	35.14		$7 \pm 4$	Unclassified
20	1 10 27.766	-45 22 55.10		17.74	14.94	0.983		$2.89 \pm 0.15$	0.234	3	23.39	-23.29				Absorption
21	1 10 29.774	-45 48 58.47	20.42	19.54		0.452	$0.58 \pm 0.01$		0.482	3	23.70	-23.03	35.94		$99 \pm 47$	Unclassified
22	1 10 30.175	-45 31 13.83	17.41	17.08		0.972	$0.35 \pm 0.01$		0.000	0						Star
23	1 10 32.481	-45 40 4.06	20.72	19.93	16.36	0.618	$0.83 \pm 0.05$	$3.26 \pm 0.04$	0.412	3	23.70	-22.01	34.77	$42 \pm 21$		Sy2
24	1 10 32.553	-45 54 4.38	18.73	17.94		1.920	$0.85 \pm 0.02$		0.255	3	23.76	-23.40				Absorption
25	1 10 33.353	-44 59 57.66		21.02		1.319			0.571	1	24.32	-22.55				Absorption
26	1 10 33.645	-45 40 21.17	19.80	18.75	15.43	0.306	$1.06 \pm 0.04$	$3.48 \pm 0.02$	0.410	3	23.39	-23.72	35.96		$55 \pm 20$	Star-forming
27	1 10 34.006	-45 51 20.19	21.04	20.61		0.248	$0.52 \pm 0.05$		0.371	3	23.21	-21.34	34.86		$39 \pm 7$	Star-forming
28	1 10 38.188	-45 38 18.78	17.77	17.30		0.257	$0.50 \pm 0.01$		0.189	3	22.62	-23.14	35.11	$33 \pm 6$	$6 \pm 2$	Star-forming
29	1 10 43.881	-45 51 22.65	20.55	20.22		0.198	$0.22 \pm 0.05$		0.210	3	22.60	-20.42	33.95	$28 \pm 6$	$38 \pm 12$	Star-forming
30	1 10 47.157	-45 16 17.33		15.57		1.259			0.000	0						Star
31	1 10 52.007	-45 43 39.89	20.20	20.03		0.182	$0.59 \pm 0.04$		0.373	3	23.08	-21.93	34.69		$15 \pm 9$	Star-forming
32	1 10 52.185	-45 33 54.00	19.23	18.55		0.425	$0.57 \pm 0.02$		0.122	3	22.45	-20.90	34.25	$36 \pm 10$	$2 \pm 2$	Star-forming
33	1 10 53.150	-46 7 0.92	16.61	15.98		8.740	$0.66 \pm 0.01$		0.102	3	23.61	-23.08				Absorption
34	1 10 55.062	-45 6 37.52		18.98		1.045			0.377	1	23.85	-23.27				Absorption
35	1 10 55.776	-45 39 19.86	16.22	15.74	14.10	0.315	$0.47 \pm 0.01$	$1.93 \pm 0.02$	0.024	3	20.90	-20.05	33.97	$41 \pm 3$		Star-forming
36	1 10 57.095	-45 52 10.68	22.57	21.22		0.840	$1.07 \pm 0.16$		0.693	1	24.30	-23.16				Absorption
37	1 11 1.711	-45 41 57.47	19.60	18.98		0.246	$0.64 \pm 0.03$		0.282	3	22.96	-22.43	35.08		$23 \pm 9$	Star-forming
38	1 11 2.237	-46 18 23.88	18.70	22.67		0.712	$0.66 \pm 0.01$		0.135	3	22.77	-17.05				Absorption
39	1 11 2.685	-46 27 43.06	21.32	19.98		0.773	$1.28 \pm 0.09$		0.574	2	24.10	-23.72				Absorption
40	1 11 5.203	-45 38 49.91	22.26	20.79	17.19	0.124	$1.07 \pm 0.14$	$3.92 \pm 0.08$	0.538	3	23.24	-22.32	34.75		$12 \pm 5$	Unclassified
41	1 11 6.069	-45 49 18.60	18.18	17.71		0.303	$0.48 \pm 0.01$		0.126	3	22.33	-21.78	34.90	$71 \pm 3$	$19 \pm 7$	Star-forming
42	1 11 8.803	-45 36 22.32	17.71	17.18		0.226	$0.49 \pm 0.01$		0.090	3	21.91	-21.54	34.58	$42 \pm 7$		Star-forming
43	1 11 10.035	-46 10 11.43	18.96	18.20		0.410	$0.78 \pm 0.02$		0.231	3	23.00	-22.88				Absorption

Table 1: continued

#		RA (J2000)	Dec (J2000)	$m_V$	$m_R$	$m_K$	$S_{1.4}$ (mJy)	$V - R$	$R - K$	$z$	$Q$	$\log P_{1.4}$ (W/Hz)	$M_R$	$\log L_{H\alpha}$ (W)	$EW_{H\alpha}$ (Å)	$EW_{[O\ III] \lambda 777}$ (Å)	class		
44	1	11	12.628	-45	51	12.80	21.88	20.89	16.86	0.154	$0.83 \pm 0.09$	$4.03 \pm 0.08$	0.551	3	23.36	-22.07	34.60	$11 \pm 6$	Star-forming
45	1	11	14.985	-45	32	13.73	19.81	18.79		0.219	$0.94 \pm 0.03$		0.301	3	22.97	-22.96			Absorption
46	1	11	15.979	-46	9	38.13	20.29	19.98		3.202	$0.23 \pm 0.05$		1.058	1	25.27	-23.99			Sy1
47	1	11	15.834	-45	43	41.99	22.22	20.75		0.222	$0.88 \pm 0.10$		0.695	1	23.73	-23.33			Absorption
48	1	11	21.231	-45	44	30.37	20.43	19.68	17.17	0.144	$0.43 \pm 0.04$	$2.48 \pm 0.08$	0.301	3	22.78	-21.78	34.81	$23 \pm 13$	Star-forming
49	1	11	23.731	-45	43	43.56	20.68	20.09	16.58	0.351	$0.56 \pm 0.06$	$3.48 \pm 0.06$	0.332	3	23.26	-21.40	35.05	$58 \pm 32$	Sy2?
50	1	11	26.248	-45	38	14.60	18.19	17.75	15.66	0.419	$0.66 \pm 0.01$	$2.43 \pm 0.15$	0.125	3	22.47	-21.78			Absorption
51	1	11	26.377	-45	30	17.04	20.83	19.69		0.323	$0.94 \pm 0.07$		0.422	2	23.44	-22.73	34.52	$5 \pm 4$	Unclassified
52	1	11	26.906	-45	34	16.26	19.10	18.57		0.141	$0.46 \pm 0.02$		0.190	3	23.36	-21.86	34.71	$43 \pm 12$	Star-forming
53	1	11	27.490	-45	49	45.56	19.11	18.58		0.225	$0.53 \pm 0.02$		0.343	3	23.09	-23.19	34.92	$8 \pm 3$	Star-forming
54	1	11	27.584	-45	48	14.88	19.36	18.51		0.438	$0.67 \pm 0.02$		0.279	3	23.20	-22.91	34.69	$6 \pm 4$	Star-forming
55	1	11	28.464	-45	54	8.47	20.35	19.69	16.40	0.144	$0.69 \pm 0.06$	$3.47 \pm 0.06$	0.299	3	22.78	-21.88	34.71	$42 \pm 15$	Star-forming
56	1	11	29.525	-45	52	42.27	22.82	21.34		0.171	$1.55 \pm 0.17$		0.553	1	23.41	-22.51			Absorption
57	1	11	30.481	-45	37	25.35	18.33	17.86		0.202	$0.51 \pm 0.02$		0.177	3	22.46	-22.43	34.58	$19 \pm 7$	Star-forming
58	1	11	32.877	-45	17	57.00		17.72		0.333			0.126	3	22.37	-21.82	34.54	$29 \pm 3$	Star-forming
59	1	11	34.149	-45	46	8.58	20.44	19.35	15.92	0.199	$0.86 \pm 0.04$	$3.39 \pm 0.03$	0.420	3	23.22	-22.64	35.08	$20 \pm 10$	Sy2
60	1	11	35.073	-45	32	44.81	16.62	15.99		0.172	$0.61 \pm 0.01$		0.089	3	21.78	-22.75	34.41	$9 \pm 2$	Star-forming
61	1	11	36.135	-45	34	24.33	19.60	19.02		0.331	$0.89 \pm 0.03$		0.376	3	23.34	-22.73	34.97	$14 \pm 4$	Sy2?
62	1	11	36.333	-45	42	48.81	20.38	19.70		0.266	$0.55 \pm 0.04$		0.271	3	22.96	-21.57	34.94	$38 \pm 11$	Unclassified
63	1	11	38.309	-45	33	57.14	21.43	20.80		0.163	$0.79 \pm 0.09$		0.670	3	23.56	-22.19	35.31	$50 \pm 13$	Sy2
64	1	11	39.411	-45	16	16.88		19.02		4.294			0.377	3	24.46	-23.24			Absorption
65	1	11	40.335	-45	47	12.29	19.43	18.96	16.18	0.549	$0.39 \pm 0.02$	$2.93 \pm 0.03$	2.239	2	25.19	-26.58			Sy1
66	1	11	44.660	-45	52	11.48	19.46	18.84		0.458	$0.65 \pm 0.02$		0.298	3	23.28	-22.41	35.30	$40 \pm 8$	Sy2?
67	1	11	49.622	-45	42	6.90	21.59	21.01	17.19	0.224	$1.11 \pm 0.03$	$3.77 \pm 0.07$	0.743	1	23.79	-23.85			Unclassified
68	1	11	49.644	-45	54	13.56	22.04	21.23		0.140	$0.61 \pm 0.20$		0.670	3	23.49	-22.39	34.94	$18 \pm 5$	Unclassified
69	1	11	50.235	-45	37	26.65	20.23	19.29	15.90	0.255	$1.08 \pm 0.05$	$3.46 \pm 0.03$	0.493	3	23.48	-23.58	35.54	$23 \pm 7$	Unclassified
70	1	11	51.234	-45	2	14.60		18.10		2.553			0.272	3	23.94	-23.31			Absorption
71	1	11	51.508	-45	44	43.70	22.01	21.20	19.10	0.154	$0.68 \pm 0.09$	$2.26 \pm 0.18$	0.496	3	23.26	-21.45			Star-forming
72	1	11	52.850	-45	40	24.21	19.95	19.24		0.221	$0.69 \pm 0.04$		0.228	3	22.72	-21.75	34.16	$13 \pm 4$	Star-forming
73	1	11	53.502	-45	58	46.41	17.21	16.69	14.68	0.181	$0.57 \pm 0.01$	$1.95 \pm 0.20$	0.026	3	20.73	-19.27	33.54	$31 \pm 2$	Sy2?
74	1	11	54.203	-45	30	39.58	20.62	19.06	15.76	0.295	$1.35 \pm 0.06$	$3.46 \pm 0.04$	0.449	3	23.45	-23.85			Absorption
75	1	11	54.267	-45	54	8.85	18.92	18.24	15.17	0.225	$0.67 \pm 0.02$	$2.99 \pm 0.16$	0.136	3	22.27	-21.50	34.60	$45 \pm 5$	Star-forming
76	1	11	54.599	-45	46	38.29	21.09	20.11	16.68	0.210	$0.83 \pm 0.07$	$3.51 \pm 0.06$	0.342	3	23.06	-21.83			Absorption
77	1	11	55.250	-45	42	13.58	18.64	18.02		0.260	$0.56 \pm 0.01$		0.229	3	22.80	-22.89	35.10	$41 \pm 8$	Star-forming
78	1	11	56.684	-44	54	50.08		18.08		0.734			1.053	3	24.63	-25.88			Sy1
79	1	11	56.701	-45	47	53.99	20.91	20.18	16.15	0.152	$0.89 \pm 0.06$	$3.82 \pm 0.06$	0.721	3	23.60	-24.12	35.47	$12 \pm 2$	Star-forming
80	1	11	58.744	-45	52	10.11	20.95	20.36	16.94	0.182	$0.57 \pm 0.07$	$3.18 \pm 0.07$	1.240	3	24.17	-23.95			Sy1
81	1	12	4.050	-45	59	15.24	21.31	20.12		0.418	$1.21 \pm 0.08$		0.492	3	23.69	-22.90			Absorption
82	1	12	4.638	-45	44	47.99	19.08	18.34		0.346	$0.62 \pm 0.02$		0.255	3	23.02	-22.85	34.74	$18 \pm 5$	Unclassified
83	1	12	6.042	-45	46	27.13	20.47	19.30		0.236	$1.12 \pm 0.04$		0.000	0					Star
84	1	12	6.345	-44	49	44.96		16.70		0.885			0.082	3	22.42	-21.75	34.19	$14 \pm 2$	Sy2
85	1	12	10.694	-46	34	55.37	18.25	17.56		0.934	$0.73 \pm 0.01$		0.138	3	22.90	-22.24	34.47	$17 \pm 6$	Star-forming
86	1	12	10.419	-46	7	12.93	16.68	16.13		1.582	$0.55 \pm 0.01$		0.076	3	22.61	-22.23			Absorption

Table 1: continued

#	RA (J2000)	Dec (J2000)	$m_V$	$m_R$	$m_K$	$S_{1.4}$ (mJy)	$V - R$	$R - K$	$z$	$Q$	$\log P_{1.4}$ (W/Hz)	$M_R$	$\log L_{H\alpha}$ (W)	$EW_{H\alpha}$ (Å)	$EW_{[O\ III] \ 3727}$ (Å)	class
87	1 12 12.131	-45 40	50.29	20.58	19.95	16.45	0.154	$0.94 \pm 0.06$	$3.36 \pm 0.05$	0.461	3	23.20	-22.62	34.80	$10 \pm 4$	Unclassified
88	1 12 14.492	-45 8	43.68		21.06		0.654			0.328	2	23.52	-20.83	33.90	$7 \pm 5$	Absorption
89	1 12 15.217	-46 23	40.42	18.65	17.93		0.420	$0.69 \pm 0.01$		0.255	3	23.10	-23.31	34.68	$10 \pm 2$	Star-forming
90	1 12 16.493	-45 45	20.05	18.80	18.19	15.36	0.160	$0.63 \pm 0.02$	$2.97 \pm 0.16$	0.297	3	22.82	-23.32	34.97	$20 \pm 3$	Unclassified
91	1 12 17.671	-44 58	36.89		20.77		1.727			0.703	2	24.63	-23.67			Absorption
92	1 12 19.102	-45 53	18.37	15.86	15.28		0.868	$0.45 \pm 0.01$		0.027	3	21.44	-20.77	34.65	$101 \pm 9$	Star-forming
93	1 12 20.133	-46 37	17.83	20.05	19.42		0.375	$0.71 \pm 0.04$		0.427	3	23.51	-22.86	35.37	$32 \pm 9$	Star-forming
94	1 12 24.273	-44 55	34.22		16.05		0.934			0.033	3	21.65	-20.46	34.24	$51 \pm 3$	Star-forming
95	1 12 24.839	-45 52	32.96	20.85	19.53		0.424	$1.17 \pm 0.05$		0.416	2	23.54	-23.05	34.86	$8 \pm 5$	Unclassified
96	1 12 25.208	-45 47	0.05	18.92	18.43		0.225	$0.42 \pm 0.02$		0.236	3	22.76	-22.48	35.41	$121 \pm 11$	Star-forming
97	1 12 27.662	-45 32	8.32	16.44	15.66		3.165	$0.77 \pm 0.01$		0.000	0					Star
98	1 12 28.684	-45 49	59.78	20.91	20.37	16.05	0.236	$0.71 \pm 0.09$	$4.16 \pm 0.07$	0.298	3	22.99	-21.20	34.18	$9 \pm 7$	Unclassified
99	1 12 29.203	-46 23	49.64	18.92	18.25		0.295	$0.68 \pm 0.02$		0.210	3	22.77	-22.54			Absorption
100	1 12 29.810	-44 53	37.39		19.11		1.076			0.890	1	24.64	-26.33	36.23	$9 \pm 3$	Unclassified
101	1 12 31.607	-44 58	36.54		16.11		0.685			0.082	3	22.31	-22.43	35.13	$65 \pm 8$	Star-forming
102	1 12 32.044	-46 5	56.54	20.31	19.85		4.707	$0.57 \pm 0.05$		2.240	2	26.13	-25.69			Sy1
103	1 12 32.121	-45 8	33.59		19.74		0.285			0.378	3	23.28	-22.02	34.90	$22 \pm 8$	Sy2
104	1 12 35.667	-44 55	7.53		20.49		0.203			0.540	1	23.46	-22.86			Absorption
105	1 12 36.468	-45 18	42.14	18.27	17.27		2.064	$0.82 \pm 0.02$		0.235	3	23.72	-23.86			Absorption
106	1 12 41.313	-46 3	23.27	19.95	19.36		0.351	$0.38 \pm 0.03$		0.313	3	23.21	-22.18	35.20	$40 \pm 10$	Star-forming
107	1 12 41.432	-46 3	58.29	22.33	21.63		0.390	$1.14 \pm 0.19$		0.698	2	23.98	-22.95	35.44	$32 \pm 19$	Unclassified
108	1 12 41.800	-45 37	6.58	18.58	17.70		0.862	$0.80 \pm 0.02$		0.234	3	23.34	-23.41			Absorption
109	1 12 43.743	-45 37	43.63	19.27	18.59		0.401	$0.79 \pm 0.02$		0.235	3	23.01	-22.53			Absorption
110	1 12 44.277	-45 33	14.99	22.38	21.26		0.399	$1.45 \pm 0.20$		0.539	2	23.75	-22.33	34.19	$3 \pm 3$	Absorption
111	1 12 47.347	-46 13	22.93	21.25	20.92		0.464	$0.34 \pm 0.06$		0.816	2	24.19	-22.49	34.92	$15 \pm 4$	Sy1
112	1 12 47.858	-45 44	50.12	19.23	18.30		0.860	$0.82 \pm 0.04$		0.239	3	23.35	-22.88	34.59	$12 \pm 4$	Unclassified
113	1 12 52.643	-45 43	44.88	16.09	15.43		1.584	$0.66 \pm 0.03$		0.076	3	22.61	-22.95			Absorption
114	1 12 55.584	-45 59	6.13	20.31	19.47		0.373	$0.68 \pm 0.05$		0.445	3	23.55	-22.90	35.30	$26 \pm 9$	Star-forming
115	1 13 3.882	-45 30	8.77	16.99	16.42		0.305	$0.54 \pm 0.01$		0.086	3	22.00	-22.21	34.60	$24 \pm 2$	Star-forming
116	1 13 5.996	-46 26	3.38	17.62	17.18		0.736	$0.44 \pm 0.01$		0.066	3	22.15	-20.84	34.65	$96 \pm 6$	Star-forming
117	1 13 8.171	-45 57	49.65	20.84	19.74		0.497	$1.15 \pm 0.06$		0.447	3	23.68	-22.38	34.92	$17 \pm 3$	Sy2
118	1 13 10.512	-44 50	5.56		17.37		0.489			0.000	0					Star
119	1 13 10.973	-45 1	45.49		16.37	14.69	0.643		$1.81 \pm 0.20$	0.081	3	22.27	-22.05	34.88	$52 \pm 5$	Sy2?
120	1 13 13.758	-46 1	56.63	16.60	15.95	13.42	0.578	$0.72 \pm 0.01$	$2.54 \pm 0.17$	0.134	3	22.67	-23.77			Absorption
121	1 13 14.689	-45 37	0.95	20.14	18.98		0.400	$1.10 \pm 0.04$		0.368	3	23.41	-23.29			Absorption
122	1 13 15.269	-45 45	23.70	22.16	21.06		0.242	$0.74 \pm 0.11$		0.368	1	23.19	-20.94	34.42	$20 \pm 13$	Unclassified
123	1 13 15.700	-44 59	19.03		17.34	14.62	0.444		$2.40 \pm 0.15$	0.235	3	23.05	-23.40	35.33	$42 \pm 7$	Sy2?
124	1 13 21.199	-46 12	41.45	21.85	21.42		0.403	$0.65 \pm 0.11$		0.818	3	24.13	-23.19	35.29	$19 \pm 9$	Unclassified
125	1 13 23.325	-46 11	31.93	19.30	18.53		0.442	$0.66 \pm 0.02$		0.158	3	22.70	-21.35	34.08	$16 \pm 2$	Sy2
126	1 13 25.180	-46 15	32.55	19.11	18.14		0.858	$0.78 \pm 0.02$		0.164	2	23.02	-22.11			Absorption
127	1 13 25.888	-45 49	10.08	18.22	17.73		0.508	$0.54 \pm 0.01$		0.252	3	23.17	-23.39	35.29	$40 \pm 10$	Star-forming
128	1 13 26.987	-46 24	22.45	18.90	18.05		0.902	$0.83 \pm 0.02$		0.254	3	23.43	-23.27	34.74	$5 \pm 5$	Absorption
129	1 13 29.537	-45 37	18.43	22.60	20.90		0.546	$1.40 \pm 0.21$		0.693	3	24.12	-24.10			Absorption

Table 1: continued

#	RA (J2000)	Dec (J2000)	$m_V$	$m_R$	$m_K$	$S_{1.4}$ (mJy)	$V - R$	$R - K$	$z$	$Q$	$\log P_{1.4}$ (W/Hz)	$M_R$	$\log L_{H\alpha}$ (W)	$EW_{H\alpha}$ (Å)	$EW_{[O\ III] \ 3727}$ (Å)	class
130	1 13 29.657	-45 45 33.63	22.07	21.12		0.267	$0.98 \pm 0.09$		0.650	2	23.75	-22.74	34.73		$8 \pm 5$	Unclassified
131	1 13 30.919	-45 21 21.43	19.32	18.25		0.755	$0.99 \pm 0.02$		0.327	3	23.58	-23.70				Absorption
132	1 13 31.745	-46 2 5.99	16.43	15.93		0.484	$0.52 \pm 0.01$		0.090	3	22.24	-22.80	34.80	$22 \pm 3$		Star-forming
133	1 13 33.360	-45 38 40.80	19.39	18.47		0.450	$0.96 \pm 0.02$		0.276	3	23.20	-23.11	35.68	$121 \pm 41$	$91 \pm 22$	Star-forming
134	1 13 38.678	-45 2 58.65		20.45		0.236			0.414	1	23.28	-22.06	34.02		$3 \pm 1$	Unclassified
135	1 13 46.657	-46 4 40.28		17.51		4.061			0.095	3	23.21	-21.37				Absorption
136	1 13 49.218	-45 40 50.65		19.96		0.290			1.837	2	24.73	-25.17				Sy1
137	1 13 49.792	-46 15 52.39		15.29		0.520			0.000	0						Star
138	1 13 53.285	-44 53 34.90		16.52		1.754			0.147	3	23.23	-23.39				Absorption
139	1 13 55.065	-45 27 15.80		15.51		2.428			0.090	3	22.94	-23.25				Absorption
140	1 13 57.032	-45 47 32.52	18.83	17.86		1.157	$0.95 \pm 0.01$		0.000	0						Star
141	1 14 0.588	-45 47 52.12	18.98	18.50		0.194	$0.45 \pm 0.02$		0.071	3	21.64	-19.68	33.26	$11 \pm 2$		Star-forming
142	1 14 3.261	-45 52 22.47		20.14		0.520			0.566	3	23.91	-23.40				Absorption
143	1 14 4.663	-45 57 0.45		19.50		1.041			0.374	3	23.84	-22.74				Absorption
144	1 14 5.861	-45 6 50.91		17.67		0.489			0.076	3	22.10	-20.70	34.52	$79 \pm 7$		Star-forming
145	1 14 6.790	-45 54 19.07		20.00		1.496			0.000	0						Star
146	1 14 7.604	-45 14 47.89		15.51		20.318			0.089	3	23.85	-23.22				Absorption
147	1 14 8.364	-44 56 47.94		17.11		0.862			0.253	3	23.41	-24.12				Absorption
148	1 14 8.840	-44 48 50.03		16.42		1.555			0.147	3	23.18	-23.49				Absorption
149	1 14 9.484	-45 32 44.56		19.96		0.475			0.596	3	23.92	-23.79	35.23		$9 \pm 4$	Unclassified
150	1 14 14.654	-45 19 51.69		16.31		1.697			0.123	3	23.06	-23.02	34.71	$14 \pm 2$	$7 \pm 3$	Sy2
151	1 14 15.662	-45 31 47.72		16.88		0.461			0.077	3	22.08	-21.52	34.82	$73 \pm 3$	$17 \pm 2$	Star-forming
152	1 14 19.430	-45 31 53.98		20.01		0.285			0.827	3	23.99	-23.44	35.20		$12 \pm 2$	Sy1
153	1 14 22.999	-45 34 29.89		21.37		1.675			0.656	3	24.55	-22.78	35.89		$109 \pm 33$	Unclassified
154	1 14 25.193	-45 4 48.11		15.60		1.317			0.122	3	22.94	-23.86	34.62	$5 \pm 1$		Star-forming
155	1 14 26.518	-45 52 22.87		18.89		0.331			0.459	3	23.52	-23.92	35.62		$21 \pm 7$	Unclassified
156	1 14 28.439	-45 36 36.96		19.47		0.929			0.406	3	23.86	-22.99	35.11		$15 \pm 4$	Star-forming
157	1 14 28.841	-45 28 21.36		21.16		2.050			0.693	1	24.69	-23.22				Absorption
158	1 14 32.932	-45 24 1.18		18.76		0.375			0.333	3	23.29	-23.16	35.61		$40 \pm 11$	Star-forming
159	1 14 36.756	-44 51 26.45		19.73		2.479			0.380	3	24.23	-22.04	35.15		$39 \pm 12$	Sy2
160	1 14 38.885	-45 40 27.18		21.18		1.258			0.662	1	24.44	-23.01				Absorption
161	1 14 43.078	-45 54 16.21		20.75		1.027			0.526	2	24.14	-22.51	35.49		$55 \pm 18$	Unclassified
162	1 14 48.708	-45 30 47.24		18.83		0.296			0.236	3	22.88	-22.22	34.85	$41 \pm 15$	$14 \pm 4$	Star-forming
163	1 14 53.790	-45 58 21.32		17.53		0.670			0.236	3	23.23	-23.53	35.28	$33 \pm 4$	$11 \pm 6$	Star-forming
164	1 14 54.050	-45 47 5.45		19.21		0.314			0.216	3	22.83	-21.63	34.36	$23 \pm 6$	$7 \pm 2$	Star-forming
165	1 14 56.034	-46 17 59.27		18.32		0.207			0.253	3	22.79	-22.91				Absorption
166	1 14 57.836	-45 6 15.37		19.18		0.706			0.334	3	23.57	-22.74	35.29	$70 \pm 5$	$9 \pm 3$	Star-forming
167	1 14 59.895	-44 57 57.68		18.05		1.985			0.224	3	23.66	-22.58	34.82	$28 \pm 3$	$7 \pm 2$	Sy2?
168	1 15 1.969	-45 44 52.55		20.96		0.632			0.757	3	24.26	-23.80	35.69		$27 \pm 10$	Star-forming
169	1 15 2.579	-45 36 6.14		19.31		0.160			0.000	0						Star
170	1 15 4.930	-45 49 44.53		20.88		0.467			0.000	0						Star
171	1 15 9.783	-45 24 7.89		20.79		0.345			0.317	3	23.21	-21.00				Absorption
172	1 15 13.275	-46 15 27.38		16.98		0.320			0.170	3	22.62	-23.28	34.43	$6 \pm 3$		Star-forming



Table 1: continued

#		RA (J2000)	Dec (J2000)	$m_V$	$m_R$	$m_K$	$S_{1.4}$ (mJy)	$V - R$	$R - K$	$z$	$Q$	$\log P_{1.4}$ (W/Hz)	$M_R$	$\log L_{H\alpha}$ (W)	$EW_{H\alpha}$ (Å)	$EW_{[O\ III] \ 3727}$ (Å)	class
173	1	15	15.043	-45	38	19.92	18.28			0.000	0						Star
174	1	15	18.819	-44	55	10.26	14.22			0.031	3	22.54	-22.15	34.99	$61 \pm 2$		Star-forming
175	1	15	21.895	-45	52	15.28	18.89			0.373	3	23.87	-23.34				Absorption
176	1	15	25.870	-45	2	46.98	19.12			0.316	3	23.88	-22.67				Absorption
177	1	15	27.067	-45	55	23.93	20.04			0.527	2	24.09	-23.23	35.21		$15 \pm 5$	Unclassified
178	1	15	27.396	-45	15	6.28	20.37			0.793	3	24.13	-24.60	35.61		$11 \pm 1$	Star-forming
179	1	15	37.863	-45	0	21.78	17.15			0.000	0						Star
180	1	15	44.832	-45	55	49.64	16.00			0.103	3	24.24	-23.07				Star-forming
181	1	15	45.413	-45	49	36.61	19.03			0.373	3	23.39	-23.20	34.36		$2 \pm 1$	Absorption
182	1	15	49.771	-45	13	10.37	17.99			0.324	3	23.94	-23.86				Absorption
183	1	15	51.952	-45	54	22.36	20.20			0.460	3	24.05	-22.61	34.32		$3 \pm 2$	Absorption
184	1	15	53.041	-45	11	42.12	20.39			0.000	0						Star
185	1	16	0.198	-45	29	13.32	17.59			0.089	3	22.25	-21.14	34.65	$72 \pm 6$		Star-forming
186	1	16	0.937	-45	51	53.49	19.87			0.512	3	24.67	-23.29				Unclassified
187	1	16	4.124	-45	50	16.50	17.94			0.371	3	23.35	-24.27				Absorption
188	1	16	4.840	-46	0	52.33	16.19			0.067	3	22.43	-21.90				Absorption
189	1	16	10.669	-45	58	22.35	14.22			0.025	3	21.64	-21.68	33.85	$7 \pm 1$		Star-forming
190	1	16	10.995	-46	4	27.92	20.41			0.512	3	23.52	-22.75	35.02		$15 \pm 5$	Unclassified
191	1	16	14.427	-45	12	4.49	18.30			0.324	3	24.27	-23.55				Absorption
192	1	16	16.730	-45	53	58.49	20.60			0.520	3	23.81	-22.62				Absorption
193	1	16	17.094	-46	3	1.91	16.81			0.201	3	23.27	-23.59	35.53	$56 \pm 6$	$23 \pm 8$	Sy2
194	1	16	20.883	-46	2	22.86	20.74			0.518	3	23.64	-22.47	34.91		$15 \pm 5$	Unclassified
195	1	16	20.941	-45	0	20.48	18.72			0.299	3	23.51	-22.93	35.19	$47 \pm 7$	$18 \pm 7$	Unclassified
196	1	16	22.756	-46	11	6.73	20.45			0.564	3	23.56	-23.07	34.68		$5 \pm 3$	Star-forming
197	1	16	24.435	-45	24	2.03	16.77			0.124	3	22.45	-22.73	35.08	$44 \pm 3$	$11 \pm 4$	Star-forming
198	1	16	25.930	-45	15	1.54	19.82			0.419	2	24.00	-22.73	35.39		$36 \pm 11$	Star-forming
199	1	16	33.839	-46	14	4.58	16.03			0.028	3	21.06	-20.11	33.84	$28 \pm 1$		Star-forming
200	1	16	34.747	-46	17	43.92	15.94			0.106	3	22.67	-23.19	35.49	$73 \pm 8$		Star-forming
201	1	16	35.953	-46	16	42.37	19.16			0.535	3	23.71	-24.16				Absorption
202	1	16	36.528	-45	30	11.01	17.25			0.179	3	22.93	-23.13	34.92	$21 \pm 3$	$3 \pm 2$	Star-forming
203	1	16	46.357	-45	38	2.12	17.99			0.076	3	22.05	-20.38	34.40	$79 \pm 3$	$8 \pm 4$	Star-forming
204	1	16	48.454	-45	7	32.11	19.37			0.455	1	25.30	-23.41				Absorption
205	1	16	52.107	-45	56	11.75	17.87			0.203	3	22.95	-22.81	35.25	$61 \pm 5$	$9 \pm 2$	Star-forming
206	1	16	54.736	-44	58	36.41	19.68			0.370	3	24.15	-22.52	35.82		$118 \pm 27$	Star-forming
207	1	16	55.531	-45	54	5.83	18.03			0.119	3	22.61	-21.37	34.39	$31 \pm 6$	$14 \pm 8$	Unclassified
208	1	16	57.782	-45	31	10.49	20.26			0.581	3	23.89	-23.38				Absorption
209	1	17	0.781	-45	58	10.16	20.82			0.806	1	24.47	-22.57				Sy1
210	1	17	1.709	-45	45	50.98	19.75			0.255	3	22.86	-21.50	34.60	$45 \pm 15$	$15 \pm 4$	Star-forming
211	1	17	7.481	-46	4	13.14	17.36			0.000	0						Star
212	1	17	11.535	-45	32	46.22	19.74			0.405	3	23.46	-22.71	34.38		$4 \pm 4$	Absorption
213	1	17	17.528	-45	37	53.91	16.65		$2.62 \pm 0.18$	0.147	3	22.55	-23.25	34.79	$14 \pm 3$	$7 \pm 3$	Unclassified
214	1	17	19.454	-45	59	58.83	18.28			0.254	3	23.34	-22.62	35.20	$65 \pm 9$		Sy2?
215	1	17	20.911	-44	59	24.03	21.09			0.792	3	25.78	-23.89	35.51		$16 \pm 6$	Unclassified

Table 1: continued

#		RA (J2000)	Dec (J2000)	$m_V$	$m_R$	$m_K$	$S_{1.4}$ (mJy)	$V - R$	$R - K$	$z$	$Q$	$\log P_{1.4}$ (W/Hz)	$M_R$	$\log L_{H\alpha}$ (W)	$EW_{H\alpha}$ (Å)	$EW_{[O\ III] \ 3727}$ (Å)	class
216	1	17	22.319	-45	33	10.05	19.88			0.146	3	22.84	-20.01	33.95	$40 \pm 15$	$69 \pm 64$	Unclassified
217	1	17	22.600	-45	50	22.57	16.38			0.125	3	22.37	-23.13				Absorption
218	1	17	25.395	-46	5	47.74	16.80			0.090	3	22.53	-21.96	34.95	$66 \pm 9$		Star-forming
219	1	17	27.019	-45	28	15.41	19.45			0.331	3	23.35	-22.46	35.08	$56 \pm 29$	$17 \pm 7$	Star-forming
220	1	17	30.572	-46	6	39.98	19.83			0.527	3	24.14	-23.44	34.89		$6 \pm 3$	Star-forming
221	1	17	31.186	-45	38	20.02	20.49			0.536	3	23.74	-22.83				Absorption
222	1	17	32.897	-46	11	25.83	17.58			0.236	3	22.95	-23.48				Absorption
223	1	17	35.683	-45	28	58.65	18.24			0.173	3	22.94	-22.06	34.97	$64 \pm 3$	$14 \pm 2$	Star-forming
224	1	17	36.113	-45	39	34.05	18.26	15.48	$2.83 \pm 0.16$	0.159	3	22.79	-21.83	34.64	$36 \pm 12$	$8 \pm 4$	Star-forming
225	1	17	41.684	-46	11	3.26	16.55			0.104	3	22.29	-22.53	34.98	$42 \pm 0$		Unclassified
226	1	17	44.486	-45	53	34.69	21.42			0.652	3	23.97	-22.71	35.85		$106 \pm 16$	Unclassified
227	1	17	52.773	-45	31	3.33	17.34			0.146	3	23.01	-22.55	35.09	$52 \pm 5$	$7 \pm 4$	Unclassified
228	1	17	54.361	-45	43	42.85	17.73			0.000	0						Star
229	1	17	54.996	-45	51	23.27	17.91			0.238	3	22.96	-22.85	34.82	$22 \pm 4$	$4 \pm 2$	Sy2?
230	1	18	1.025	-45	38	29.06	17.06			0.000	0						Star
231	1	18	4.647	-45	58	6.97	20.77			0.803	3	24.66	-24.26	35.04		$4 \pm 1$	Unclassified
232	1	18	6.828	-45	19	1.65	18.43			0.301	3	23.67	-23.23				Absorption
233	1	18	10.074	-45	34	20.70	17.39			0.192	3	23.40	-23.16				Absorption
234	1	18	11.767	-46	9	55.55	17.98			0.492	2	24.37	-25.04				Unclassified
235	1	18	12.110	-45	45	24.45	18.97			0.370	3	24.27	-23.23	35.47		$27 \pm 7$	Star-forming
236	1	18	20.756	-45	39	38.92	15.94			0.132	3	24.27	-23.70				Absorption
237	1	18	23.871	-45	33	38.63	18.94			0.379	3	23.78	-23.33	35.37		$20 \pm 7$	Unclassified
238	1	18	28.201	-46	6	50.22	21.00			0.561	3	23.90	-22.50	34.85		$13 \pm 3$	Star-forming
239	1	18	30.444	-46	4	45.27	20.23			0.832	3	24.18	-24.96	35.46		$5 \pm 1$	Unclassified
240	1	18	30.467	-45	31	20.02	17.51			0.850	3	24.64	-26.00				Sy1
241	1	18	34.246	-45	36	38.25	17.80			0.000	0						Star
242	1	18	36.562	-45	36	24.45	18.92			0.377	3	24.01	-23.33				Absorption
243	1	18	40.904	-45	36	29.20	18.20			0.000	0						Star
244	1	19	9.827	-45	30	15.64	16.21			0.146	3	23.09	-23.68	35.35	$34 \pm 3$		Unclassified
245	1	19	19.491	-45	34	30.38	16.52			0.104	3	22.64	-22.57	34.81	$27 \pm 0$		Unclassified
246	1	19	19.885	-45	46	29.22	19.73			0.376	3	23.86	-22.52	34.46		$5 \pm 1$	Unclassified

### 3 THE CATALOGUE

The photometric (optical and near-infrared), radio, spectroscopic and intrinsic properties of the faint radio sources with established redshift are presented in Table 1, which has the following format

- (1) Radio source sequential number.
- (2-7) Right ascension and declination of the optical counterpart of the radio source in J2000.
- (8-10) Apparent ‘total’ magnitudes (section 2.2.5),  $m_V$ ,  $m_R$  and  $m_K$ , of the optical counterpart of the radio source at  $V$ ,  $R$  and  $K$  wavebands respectively.
- (11) Radio flux density at 1.4 GHz in mJy.
- (12-13)  $V-R$  and  $R-K$  colours respectively, calculated using aperture photometry (section 2.2.5) along with the associated uncertainties.
- (14) Redshift  $z$ .
- (15) Redshift estimate quality parameter,  $Q$ , defined in section 2.4.2.
- (16)  $\log_{10}$  1.4 GHz radio luminosity in  $\text{W Hz}^{-1}$ .
- (17) Absolute  $R$ -band magnitude,  $M_R$ , calculated using the ‘total’  $R$ -band apparent magnitude,  $m_R$ .
- (18)  $\log_{10}$   $H\alpha$  luminosity in  $\text{W}$ .
- (19) Rest-frame  $H\alpha$  equivalent width in  $\text{\AA}$ .
- (20) Rest-frame  $[\text{O II}] 3727$  equivalent width in  $\text{\AA}$ .
- (21) Spectral classification, described in section 4.1.

## 4 RESULTS

### 4.1 Spectral Classification

The optical counterparts of the radio sources in the sample are classified using their optical spectral features. For this purpose, we used absorption lines (Balmer lines,  $H+K$  4000  $\text{\AA}$ , G-band 4220  $\text{\AA}$ , Mgb 5175  $\text{\AA}$ , NaD 5893  $\text{\AA}$ ,  $[\text{Mg II}] 2796 \text{\AA}$ ), or the diagnostic emission line ratios (Baldwin, Phillips & Terlevich 1981; Veilleux & Osterbrock 1987; Rola, Terlevich & Terlevich 1997). This latter analysis is hampered by the low S/N of some of the spectra, the relatively poor sensitivity in the blue (affecting  $[\text{O II}] 3727$ ,  $H\beta$  4861,  $[\text{O III}] 5007$ ) and by the presence of strong atmospheric bands longward of 8000  $\text{\AA}$ , affecting  $H\alpha$  at  $z > 0.25$ . A further caveat is that stellar  $H\beta$  absorption may reduce the measured flux and equivalent width of this line. This is estimated to be  $-1.7 \pm 0.3 \text{\AA}$ , for  $z < 0.3$  radio sources (Appendix B). This correction is only approximate and might not be applicable to radio sources at  $z > 0.3$ . Ideally, knowledge of the  $H\beta$  absorption in *individual* galaxies is needed for classification purposes. Consequently, we decided not to correct for this effect and present the classification based on measured fluxes.

Diagnostic line ratios, consisting of  $H\beta/[\text{O III}] 5007$ ,  $[\text{S II}] 6716+31/H\alpha$ ,  $[\text{O I}] 6300/H\alpha$  and  $[\text{N II}] 6583/H\alpha$ , were calculated. Figure 2 shows how these ratios are used to classify the galaxies. Equal weights were assigned to each of the diagnostic line ratios available for a given object. The class assigned to the source was that consistent with the majority of the line ratios available for that source. Uncertainties in the flux calibration and dust extinction will not affect these line ratios significantly, since the pairs lie close in wavelength. However, the analysis can be applied only to objects with  $z < 0.3$ . At higher redshifts,  $H\alpha$  moves out

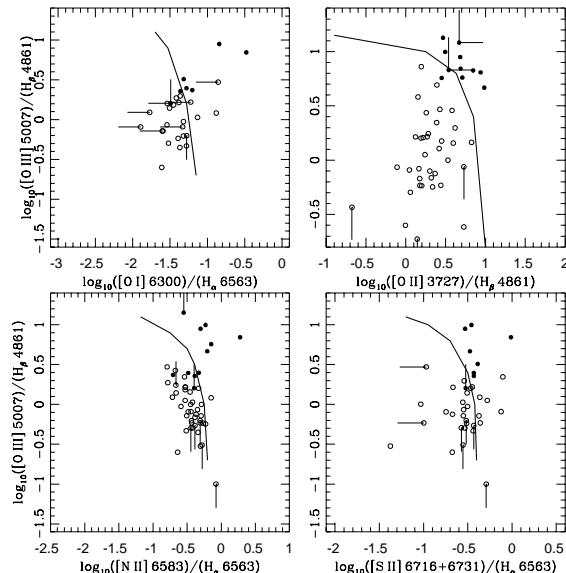


**Figure 2.** The diagnostic emission line ratios used to classify the optical counterparts of faint radio sources. The solid curves, in all panels, separate Seyferts from galaxies heated by OB stars. For the top right panel the solid curve is taken from Rola, Terlevich & Terlevich (1997), while for rest of the panels the solid curves are from Veilleux & Osterbrock (1987). Filled circles denote objects classified as Seyfert 2 type objects and open circles signify star-forming galaxies. The bars denote upper or lower limits.

of the optical window and other line ratios,  $[\text{O II}] 3727/H\beta$  and  $[\text{O III}] 5007/H\beta$ , must be employed (Rola, Terlevich & Terlevich 1997). Figure 2 shows how these ratios allow classification of the central ionizing source. However, the  $[\text{O II}] 3727/H\beta$  ratio is sensitive to both the approximate flux calibration applied to the 2dF spectra and to extinction, since it involves lines that are separated in wavelength.

The faint radio sources with redshift determination ( $\approx 70\%$  of the spectroscopic sample) were classified into four classes based on their optical spectra: (i) galaxies with only absorption lines in their spectra ( $\approx 22\%$  of the spectroscopic sample); (ii) star-forming galaxies ( $\approx 25\%$ ); (iii) Seyfert galaxies ( $\approx 9\%$ ); and (iv) unclassified objects ( $\approx 15\%$ ). The unclassified objects displayed at least one identified emission line (allowing a redshift to be determined), but the poor S/N, or a very small number of emission lines within the observable window, or the presence of instrumental features contaminating emission lines, prevented us from carrying out a reliable classification. Figure 2 shows that a large fraction of objects classified as star-forming galaxies lie close to the line delimiting Seyfert from HII-galaxy regions of the parameter space.

Class (iii) consists of ten Seyfert 1 type objects, exhibiting broad emission lines ( $\text{Ly}\alpha$  1216,  $[\text{C IV}] 1549$ ,  $[\text{C III}] 1909$ ,  $[\text{Mg II}] 2796$ ) and nineteen Seyfert 2 type galaxies. Nine of the Seyfert 2 type sources will shift to the HII region of the parameter space in Figure 2 if we correct their line ratios for the mean  $H\beta$  absorption of  $-1.7 \text{\AA}$  and the average dust extinction  $A_V=1.0$  (section 4.2) These objects are designated with a question mark in Table 1. Class (ii) includes 13 sources with absorption spectra and a single ( $H\alpha$ ) emission

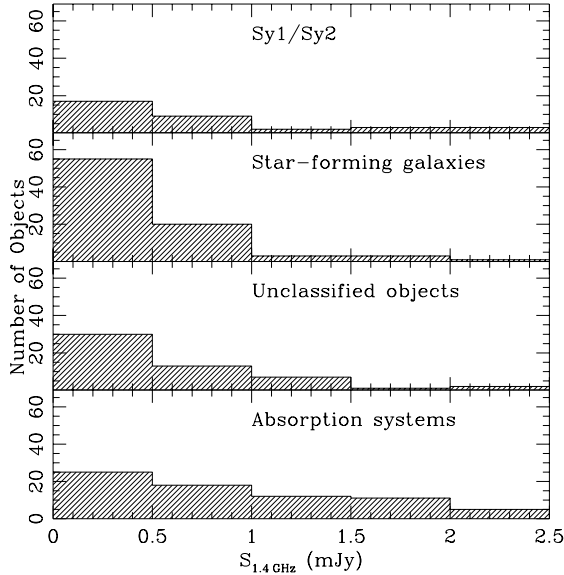


**Figure 3.** The distribution of 1.4 GHz flux density for the four optical spectroscopic classes.

line. These galaxies have a mean redshift  $z \approx 0.1$  and are likely to be early-type spirals or post-starburst galaxies. Additionally, two objects exhibiting the [Mg II] 2796 absorption feature, characteristic of extreme local starbursts (Guzman *et al.* 1997) are classified as star-forming galaxies. Finally, 18 stars are found in the sample most of which lie at large angular separations from the radio position. The fraction of radio stars contributing to the radio counts at faint flux densities is difficult to estimate, since little is known about their radio luminosity functions. Benn *et al.* (1993) found eleven stars within a sample of 87 spectroscopically observed optical identifications with  $S_{1.4} \geq 0.2$  mJy and  $m_V \leq 20$  over an effective area of  $\sim 1$  deg<sup>2</sup>. They argue that less than one radio star is expected in their sample and conclude that the rest of the stellar identifications are foreground contamination. Because the present spectroscopic sample has similar radio flux density and optical magnitude limits to that of Benn *et al.* (1993), we expect most of the stellar candidate identifications to be spurious.

The radio flux density distribution as a function of the optical classification is presented in Figure 3. Star-forming galaxies dominate at sub-mJy levels ( $S_{1.4} < 0.5$  mJy), with a small contribution ( $\approx 10\%$ ) from Seyfert galaxies. This agrees with previous studies (Benn *et al.* 1993; Kron *et al.* 1985). Absorption line systems are the dominant population at flux densities  $> 1$  mJy, although there is also a significant number at sub-mJy levels.

The apparent magnitude distribution of the optical counterparts of faint radio sources is presented in Figure 4. There is some evidence that for magnitudes  $m_R > 19.5$  mag the proportion of star-forming galaxies is decreasing relative to that of absorption line systems and Seyferts. Gruppioni *et al.* (1998), using a faint ( $S_{1.4} > 0.2$  mJy) radio sample, combined with deep ( $m_R < 22.0$  mag) spectroscopic data, also found that the majority of the optical identifications fainter than  $m_R = 20.0$  mag are absorption line systems rather than star-forming galaxies. If this trend is real, it probably re-

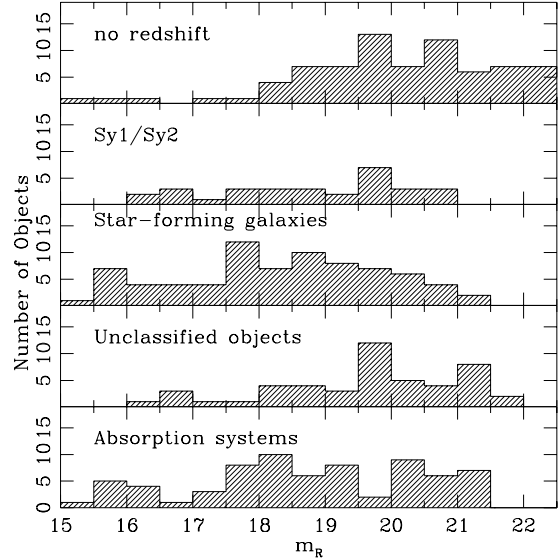


**Figure 4.** The distribution of apparent magnitude,  $m_R$ , for different classes of sources.

fects differences in the luminosity function of spirals and ellipticals.

However, it has been demonstrated that evolutionary models of giant ellipticals and QSOs, that dominate the radio population at high flux densities, cannot easily reproduce the flattening in the normalised radio source counts at sub-mJy levels (Danese *et al.* 1987; Danese, De Zotti & Franceschini 1985). Additionally, the interpretation of Figure 4 is difficult due to selection effects and incompleteness at faint optical magnitudes. A significant fraction of the faintest objects have either unclassified spectra (see section 4.5), or no redshift determination. This may modify the distribution seen in Figure 4. Furthermore, at faint optical magnitudes the classification scheme is less reliable due not only to the low S/N ratio of some of the spectra but also to the fact that fainter objects lie on average at higher redshift. As a result, not enough emission lines lie within the observable window to perform a reliable classification ([O III] 5007 redshifts outside the observable window at  $z \approx 0.65$ ).

For optical identifications with no redshift determination some information regarding their nature can be obtained using the radio-to-optical flux ratio,  $r_{1.4}$ , defined as

$$r_{1.4} = \log S_{1.4} + 0.4 m_R, \quad (3)$$

where  $S_{1.4}$ ,  $m_R$  are the radio flux and the optical apparent magnitude of sources respectively. This ratio, although distance independent, is affected by the differential optical to radio K-correction. However, this is expected to be a second order effect. In Figure 5,  $r_{1.4}$  is plotted against  $m_R$ , for all the objects detected spectroscopically. Star-forming galaxies, despite the scatter, have on average lower radio-to-optical flux ratios compared to absorption line systems at a given magnitude. Furthermore, many of the sources with no redshift determination, have  $r_{1.4}$  values higher than those of star-forming galaxies and similar to those of ellipticals. This indicates that some of these sources, are likely to be early type galaxies rather than starbursts.

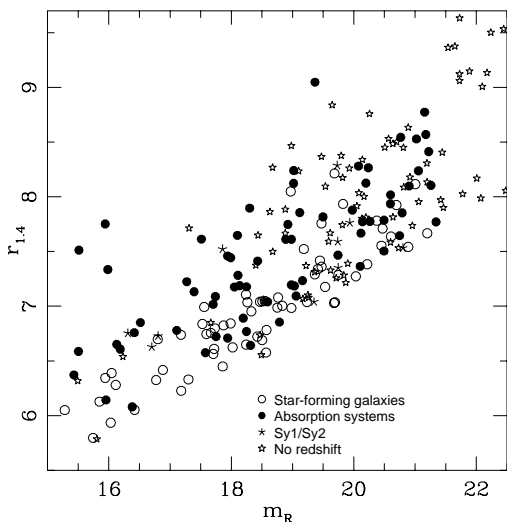


Figure 5. Radio-to-optical flux ratio versus apparent magnitude.

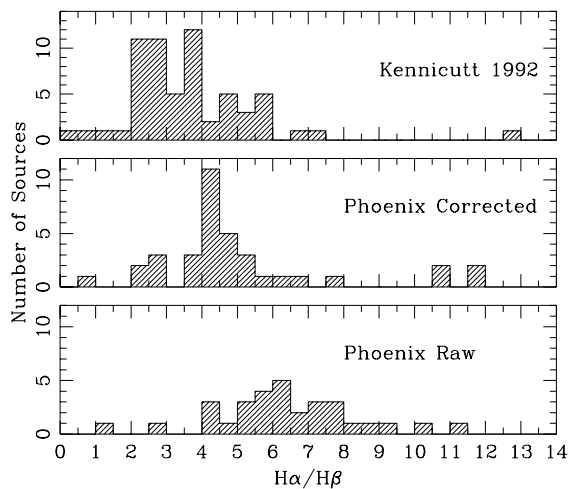


Figure 6. Distribution of the Balmer decrement for the optical counterparts of faint radio sources without correcting for  $H\beta$  absorption (bottom panel) and after accounting for that effect (middle panel). The top panel is the distribution of  $H\alpha/H\beta$  for normal galaxies (Kennicutt 1992).

## 4.2 Visual extinction from $H\alpha/H\beta$

To quantify the visual extinction,  $A_V$ , of the  $z < 0.3$  star-forming galaxies that exhibit both  $H\alpha$  and  $H\beta$  emission lines, we compare the  $H\alpha/H\beta$  decrement with the theoretical (case B recombination) value of 2.86 (Brocklehurst 1971) and a standard reddening curve (Savage & Mathis 1979). The technique is hampered by the poor S/N ratio of some of the spectra, by the uncertainties in the flux calibration (2dF data) and by stellar  $H\beta$  absorption.

Figure 6 (bottom panel) is a histogram of  $H\alpha/H\beta$ , not

corrected for stellar  $H\beta$  absorption. The distribution peaks at a value of 6, significantly below the mean value of 12 found for IRAS galaxies (Leech *et al* 1988; Elston, Cornell & Lebofsky 1985). Applying a correction of  $-1.7 \pm 0.3 \text{ \AA}$  to  $H\beta$  (Appendix B) lowers the peak of the distribution to  $\approx 4$  (Fig. 6, middle panel), consistent with  $A_V \approx 1.0 \pm 0.1$  or  $E(B - V) \approx 0.32 \pm 0.03$ . The corrected distribution implies an average dust extinction similar to that found by Kennicutt (1992) for normal galaxies (Fig. 6, top panel) and comparable to the value  $E(B - V) \approx 0.36$  obtained for disk H II regions (Kennicutt, Keel & Blaha 1989). However, the dust reddening derived here is smaller than that in nuclear H II regions ( $E(B - V) \approx 0.56$ ; Kennicutt, Keel & Blaha 1989), starburst galaxies ( $E(B - V) \approx 0.69$ ; Dahari & De Robertis 1988), IRAS sources ( $E(B - V) \approx 1.3$ ; Leech *et al* 1988; Elston, Cornell & Lebofsky 1985) and H II luminous infrared galaxies ( $E(B - V) \approx 0.99$ ; Veilleux *et al.* 1995).

It should be noted that the objects selected for spectroscopic observations are the optically brighter in the radio sample and therefore, our spectroscopic sample is biased against very dusty sources. Additionally, far-infrared and radio surveys have shown that the dust and the molecular gas in luminous infrared galaxies are generally concentrated into compact regions of diameter less than 1 kpc (Scoville *et al.* 1986, 1989, 1991; Radford *et al.* 1991). For the 2dF data, the fibre diameter of 2 arcsec corresponds to a physical size of 4 and 10 kpc at  $z=0.1$  and 0.3 respectively. This implies that the 2dF spectra sample large regions of the galaxy, which may possess a wide range of optical depths. Depending on how the regions producing the detected line and continuum emission are disposed relative to any sources of extinction, large adjustments to the extinction derived here may be required, probably in the upwards direction.

## 4.3 Colour-redshift relations

Figure 7 compares the  $V - R$  colour-redshift relation of the faint radio population with the predictions of the evolutionary models of Bruzual & Charlot (1993; see Appendix C). There is satisfactory agreement between the observed photometric indices (i.e. colours) of the faint radio sources and the completely independently classified types, based on their spectral features and diagnostic emission line ratios.

Correcting the observed optical colours using  $A_V = 1.0$  (previous section) will shift  $V - R$  bluewards by  $\approx 0.3$  magnitudes (Savage & Mathis 1979), consistent with the late-type spiral and starburst (vB; very blue) galaxy models. Such blue optical colours would imply that star-formation has not declined significantly in these galaxies since their formation, in agreement with previous studies (Benn *et al.* 1993; Kron *et al.* 1985).

The  $V - R$  and  $R - K$  colour-redshift diagrams of the sub-mJy population with  $K$ -band data are shown in Figure 8. Near-infrared ( $2.2 \mu\text{m}$ ) emission from galaxies is dominated by old stars, and is less affected by dust than is optical emission. Therefore, optical/near-infrared colours (e.g.  $R - K$ ) give information on the relative contributions from the giant and main sequence populations. Some galaxies in Figure 8 have  $V - R$  bluer than the early-type spiral (Sab/Sbc) model, but  $R - K$  colours as red as those of ellipticals. Reddening due to extinction might help to explain this apparent inconsistency. This possibility is illustrated in

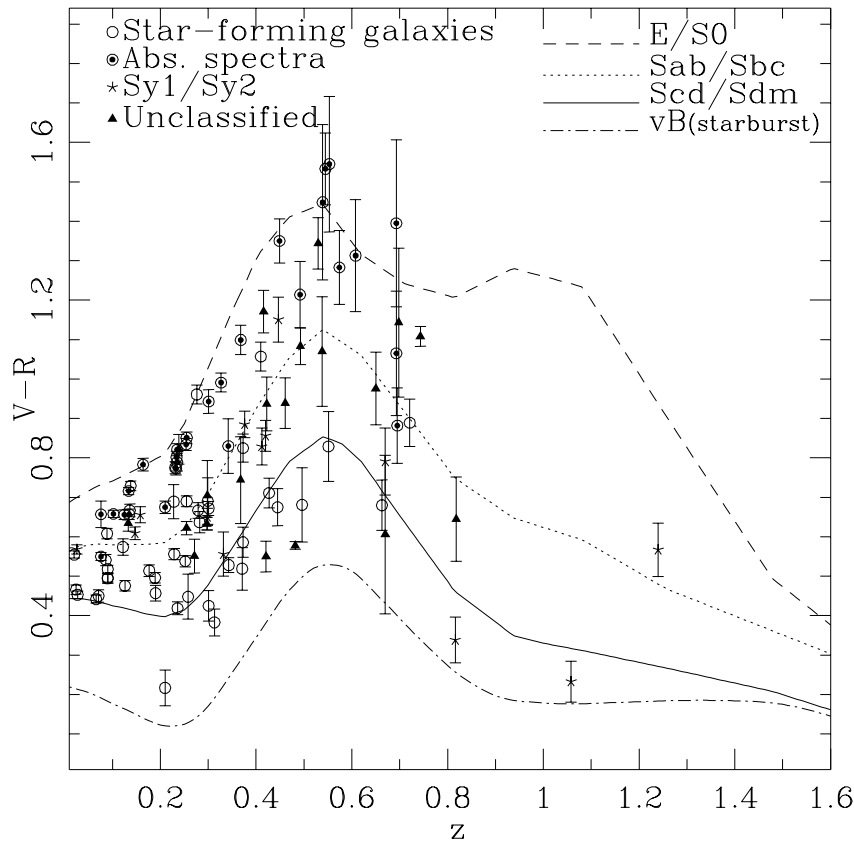


**Figure 7.** The  $V - R$  colour-redshift diagram for the faint radio population, comprising star-forming galaxies ( $\circ$ ), absorption systems ( $\odot$ ), Sy1/Sy2 objects ( $*$ ) and unclassified objects ( $\triangle$ ). The curves are based on galaxy evolution models, as explained in the text: Dashed line - E/S0 model; Dotted line - Sab/Sbc model; Continuous line - Scd/Sdm model; Dash-dotted line - starburst (vB; very blue) galaxies.

Figure 9 which compares the  $V - R$ ,  $R - K$  colour-redshift diagram with models which also include dust reddening (Savage & Mathis 1979) assuming  $A_V=1.0$ . A few galaxies still have inconsistent  $V - R$  and  $R - K$  colours which could be reconciled by adopting higher values of  $A_V$ .

Alternatively, the presence of an underlying evolved stellar population in addition to main sequence stars could explain these observations. Indications of two stellar populations (old giants and younger main sequence stars) have been found out in brighter samples of radio galaxies (‘1 Jy’ sample; Allington-Smith 1982). Lilly (1989) fit the observed broad-band spectral energy distributions (SEDs) of high-redshift radio sources using a combination of an old stellar component (age  $< 2 \times 10^9$  y) and a young population (age  $< 1 \times 10^9$  y). The young component contributes  $\approx 10\%$  to the rest frame emission at  $5000 \text{ \AA}$  and an even smaller fraction of the mass. Chambers and Charlot (1990) modelled this behaviour with a single episode of star formation lasting  $< 10^8$  years, plus a lower level of ongoing star formation. However, there are indications that the rest-frame UV and optical continuum of powerful radio sources is contaminated by both non-thermal radiation from the central engine and strong optical emission lines, undermining any

attempt to model their colours using simple stellar population synthesis models (McCarthy 1993). Nevertheless, there is some evidence that at least a fraction of the observed broad-band light of powerful radio galaxies, especially at NIR wavelengths, has stellar origin (McCarthy 1993 and reference therein). In any case, the bright radio sources studied by Lilly (1989) and Chambers & Charlot (1990) are significantly different in their nature from the fainter ones considered here and therefore, any comparison of the properties of the two populations is not straightforward.

#### 4.4 Colour-Luminosity Relations

In Figure 10 the ratio of radio to optical luminosity,  $R_{1.4}$  is plotted against the intrinsic  $V - R$  colour.  $R_{1.4}$  is defined as

$$R_{1.4} = \log P_{1.4} + 0.4 M_R, \quad (4)$$

where  $P_{1.4}$  is the radio luminosity in  $\text{WHz}^{-1}$  and  $M_R$  is the absolute  $R$ -band magnitude. Optical K-corrections are calculated using model SEDs from the population synthesis models of Bruzual & Charlot (1993) (Appendix C; section 4.6). The optical K-corrections for the Seyfert 1, 2 type galaxies in this sample were estimated using a spectral in-

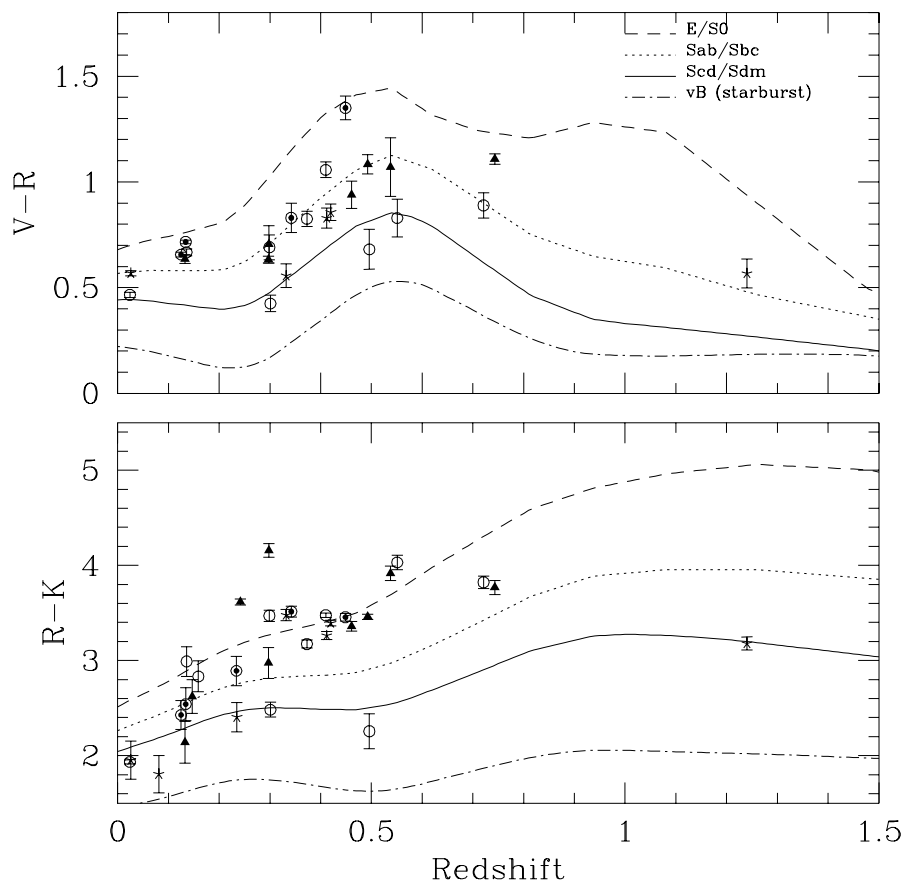


**Figure 8.**  $V - R$  and  $R - K$  colour-redshift diagrams for radio sources with near-infrared information. The symbols and the curves are defined in Figure 7.

dex of  $\alpha=-0.5$  ( $S_\nu \propto \nu^\alpha$ ). The radio luminosities were K-corrected assuming a spectral index  $\alpha=-0.8$ .

In Figure 10 there are two populations of radio sources, (i) star-forming galaxies and (ii) absorption line systems and Seyfert 1 and 2 type objects, occupying different regions of the two-colour diagram. Star-forming galaxies tend to have bluer colours for higher radio-to-optical emission. A similar result was obtained by Klein (1982) for a sample of galaxies spanning a wide range of types. The trend was interpreted as enhanced star formation in bluer galaxies, producing massive stars, that (i) contribute to the ionization of the interstellar gas and (ii) produce relativistic electrons via supernova explosions, both leading to excess radio emission (normalised to optical luminosity). To demonstrate this trend, we have constructed galaxy models with different parametric forms of the star-formation rate,  $\psi(t)$ , as a function of time (Appendix C). The star-formation rate (SFR) at a given galaxy age is related to the radio luminosity via (Condon 1992)

$$SFR(M \geq 5 M_\odot) = \frac{P_{1.4}}{4.0 \times 10^{21} \text{ W Hz}^{-1}} M_\odot \text{ yr}^{-1}. \quad (5)$$

To compare with the observations, a reddening  $A_V=1.0$  has been included in the models. The results shown in Figure

10 reproduce fairly well the observed range of colours and radio-to-optical luminosity ratios of star-forming galaxies.

A fraction of the unclassified sources in Figure 10 lie close to the region of the parameter space occupied by ellipticals and Seyfert type objects. These objects will be further discussed in the next section.

Absorption line systems exhibit a tight  $V - R$  colour dispersion. This is better demonstrated in Figure 11, presenting the colour-magnitude relation for the optical counterparts of faint radio sources. The small  $V - R$  dispersion of the absorption line systems over a wide range of optical luminosities agrees with the colour-magnitude relation (continuous line) derived for normal ellipticals in the Virgo cluster (Sandage & Visvanathan 1978). A similar result was obtained by Rixon *et al.* (1991), who also found a small dispersion ( $< 0.02$  mag) in the rest-frame  $V - R$  colours of radio selected early type galaxies with radio luminosities in the range  $24.4 < \log P_{408 \text{ MHz}} < 26.3 \text{ W Hz}^{-1}$ . On the contrary, the star-forming galaxies show significant scatter, a result that has also been found in other studies (Griessmith 1980; Schroeder 1996) and was attributed to (i) the presence of young stars and (ii) the intrinsic spread in the metallicity of galaxies.

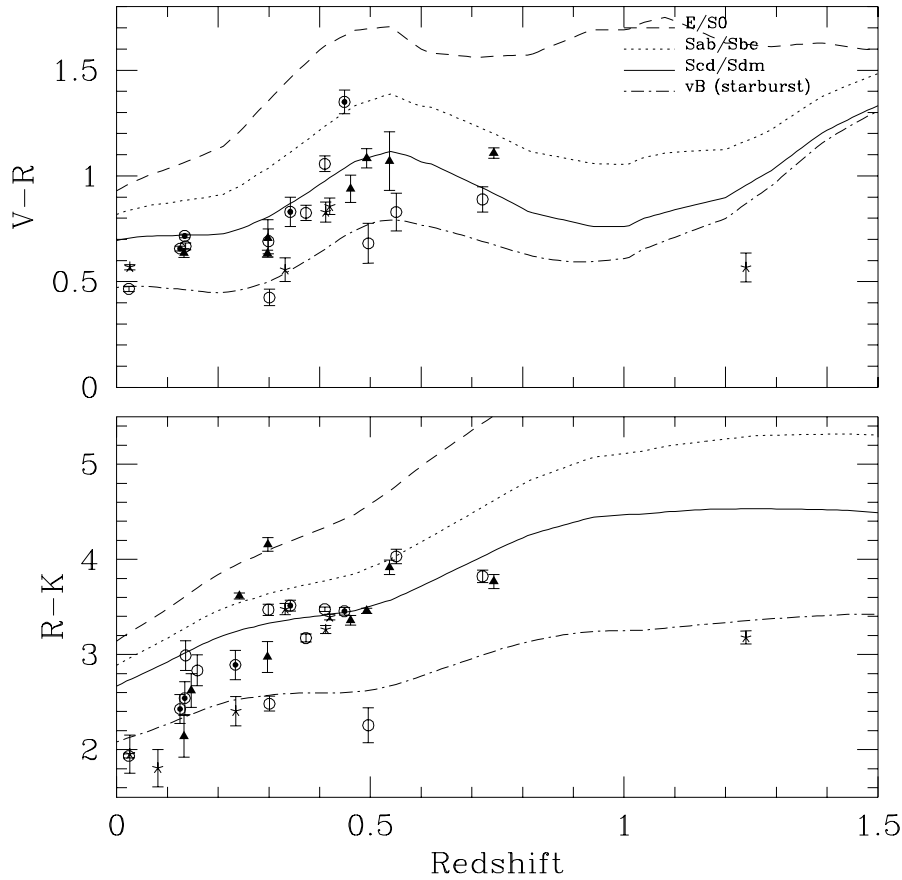


**Figure 9.** As for figure 8, with reddening ( $A_V=1.0$ ) included in the models.

#### 4.5 Radio and Optical Luminosity Distributions

Figures 12 and 13 exhibit the distributions of the radio power and the absolute optical magnitude. Optically identified faint radio sources of any type have, on average, optical luminosities in excess of  $M_R^*$  ( $M_R^* = -22.5$  mag; Metcalfe *et al.* 1991). This agrees with other studies of radio galaxies at sub-mJy flux density levels (Benn *et al.* 1993; Hammer *et al.* 1995; Windhorst *et al.* 1995). The absorption line systems (i.e. ellipticals) have optical magnitudes and radio powers in the range  $-22.0 < M_R < -24.5$  mag and  $22.0 < \log P_{1.4} < 25.0$  W Hz $^{-1}$  respectively, consistent with them being Fanaroff-Riley I types objects (Ledlow & Owen 1996). Furthermore, the distribution of these sources is tighter and peaks at a brighter luminosity both at radio (by  $\approx 1$  dex) and optical (by  $\approx 0.5$  mag) wavelengths, compared to star-forming galaxies. This latter class of objects spans the range  $-19.0 < M_R < -24.0$  mag at optical and  $20.5 < \log P_{1.4} < 24.5$  W Hz $^{-1}$  at radio wavelengths.

In Figure 12, a number of radio sources with unclassified spectra and radio power  $> 23.5$  W Hz $^{-1}$  are brighter at radio wavelengths than star-forming galaxies (their distribution peaks at  $\log P_{1.4} \approx 23.0$  W Hz $^{-1}$ ) and as bright as ellipticals or Seyfert type objects. Their median rest-frame  $V - R$  colour and radio-to-optical luminosity ratio are  $\approx 0.5$  and  $\approx 14.25$  respectively. They are the unclassified sources

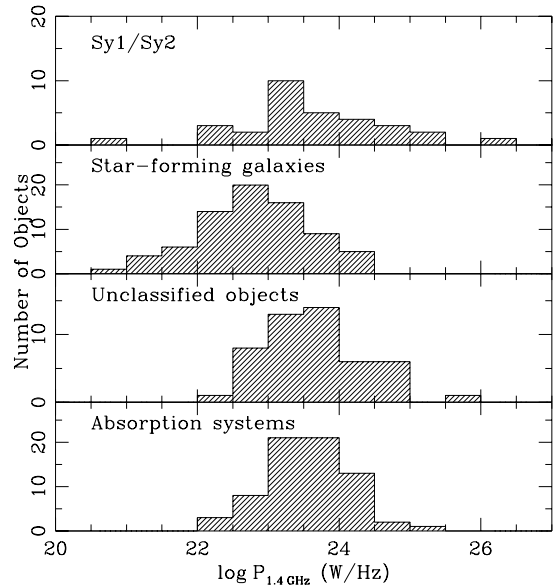


**Figure 12.** Distribution of radio powers for different classes of objects.



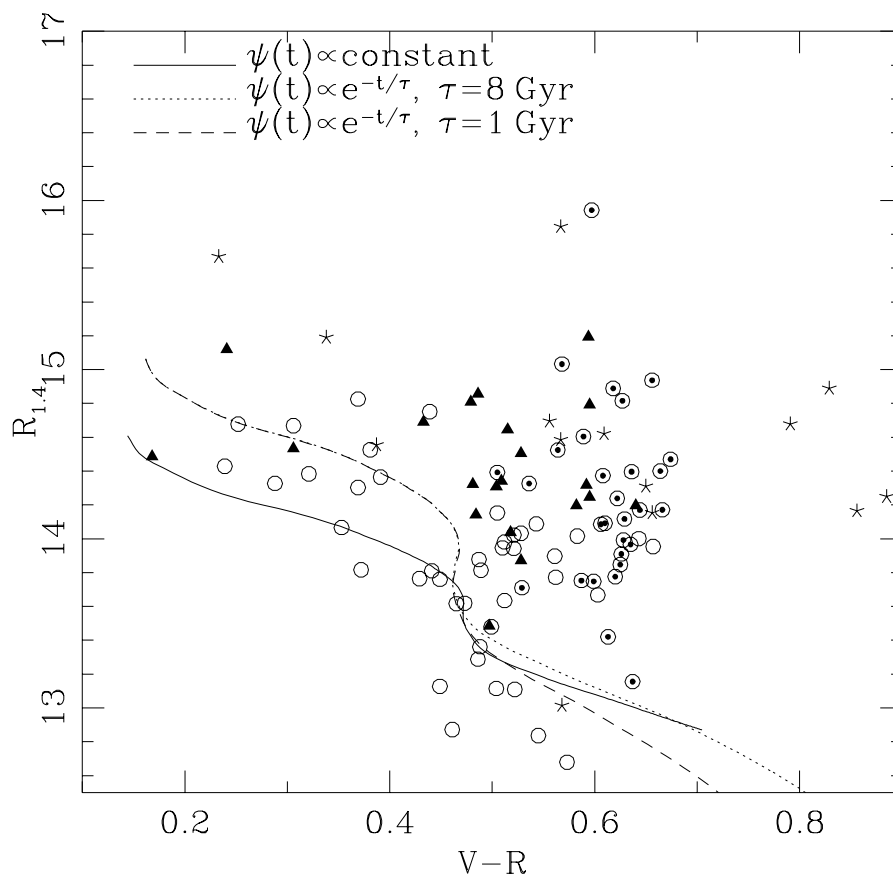


**Figure 10.** Radio-to-optical luminosity ratio against intrinsic  $V - R$  colour. The curves are models with different star-formation rates,  $\psi(t)$ , as described in the text. The symbols are the same as in Figure 7.

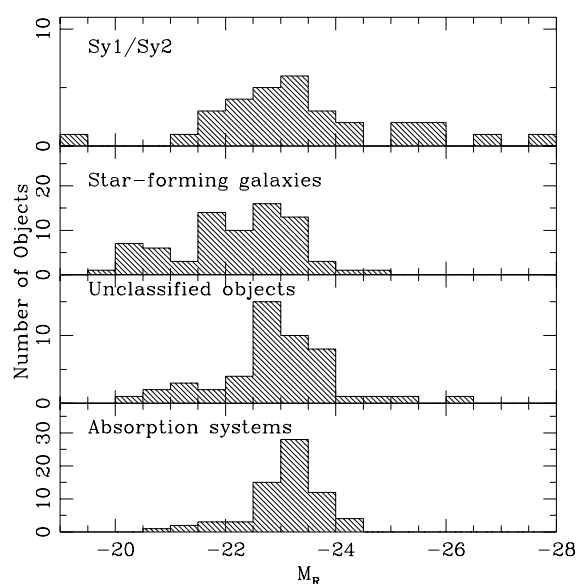


**Figure 13.** Distribution of optical luminosity for different classes of objects.

lying close to the elliptical/Seyfert region of the parameter space in Figure 10. The median redshift of these sources is  $z \approx 0.5$ , determined from only one emission line (and in some cases, one or more absorption lines), which was identified as [O II] 3727 with rest frame equivalent width of the order of  $\approx 15 \text{ \AA}$ . The evidence above indicates that a fraction of the high- $z$  unclassified sources may differ from star-forming galaxies. They might be elliptical galaxies powered by an AGN and exhibiting weak [O II] 3727 emission line, or spirals harbouring a central non-thermal source in addition to any star-formation activity.

These objects are also relatively faint ( $m_R \approx 20.0$  mag), implying that a fraction of the optically faint unclassified sources in Figure 4 (section 4.1) might be ellipticals or Seyferts rather than starbursts. However, the evidence above remains circumstantial and further spectroscopic observations are essential to investigate the nature of the central ionising source of these objects.

#### 4.6 Radio versus $H\alpha$ Luminosity

Study of the relation between  $L_{H\alpha}$  and  $P_{1.4}$  luminosities would help elucidate the link between active star-formation and radio emission in these galaxies. A relation between

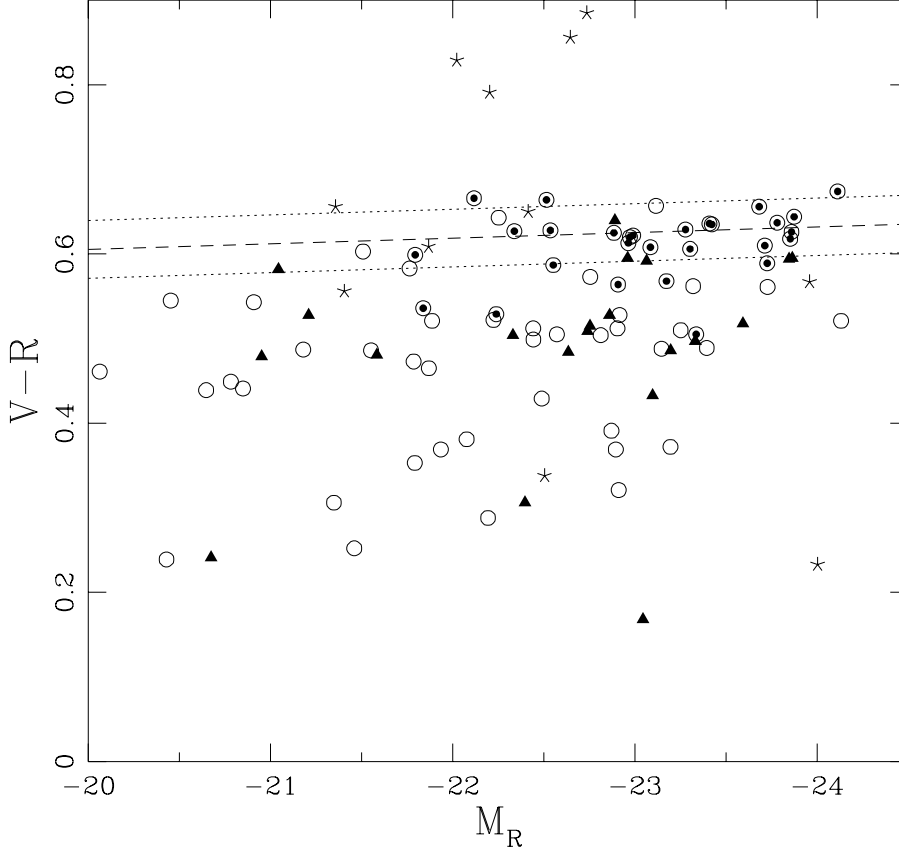


**Figure 11.** Intrinsic  $V - R$  colour against absolute  $R$ -band magnitude relation of the optical counterparts of faint radio sources. The symbols are the same as in Figure 7. Also shown are the C-M relation for ellipticals in the Virgo cluster (dashed line) along with the  $2\sigma$  envelope lines (dotted lines).

these two quantities for star-forming galaxies has already been established (Benn *et al.* 1993), suggesting that the radio luminosity is a probe of on-going star-formation in some of the sub-mJy sources.

In the absence of absolute flux calibration for the 2dF spectroscopic observations, the  $H\alpha$  luminosity is calculated using the  $R$ -band magnitudes and the measured  $H\alpha + [N II]$  equivalent widths ( $EW_{H\alpha + [N II]}$ ) of radio sources. We employ the same method to also calculate the  $H\alpha$  luminosity for the objects observed spectroscopically at ESO 3.6 m telescope. The procedure followed is summarised below.

Firstly, the absolute  $R$ -band magnitude,  $M_R$ , of a given radio galaxy is calculated from the relation

$$M_R = m_R - 5 \times \log(d_L/10) - k_R(z), \quad (6)$$

where  $d_L$  is the luminosity distance and  $k_R(z)$  is the K-correction (Yoshii & Takahara 1988). This latter is calculated using model SEDs of different galaxy types from the population synthesis code of Bruzual & Charlot (1993; Appendix C). The radio sources are assigned a model galaxy type (E/S0, Sab/Sbc, Scd/Sdm or vB), based on their position on the  $V - R$  versus redshift diagram and the corresponding K-correction is then calculated. For those objects for which only  $R$ -band data are available, we apply

the average K-correction for the Sab/Sbc SED (Appendix C). The absolute magnitude is then converted to luminosity ( $L_R$ ) using the luminosity of Vega in the  $R$ -band ( $1.869 \times 10^{-12} \text{ W m}^{-2} \text{ \AA}^{-1}$ ) and the relation

$$L_R = L_{\text{Vega}} \times 10^{(-0.4 \times M_R)}. \quad (7)$$

Finally, having established  $L_R$  and the model SED corresponding to a given radio source, we estimate, the continuum flux at  $6563 \text{ \AA}$  ( $C_{6563}$ ) from the model.  $L_{H\alpha}$  is subsequently estimated from the relation

$$L_{H\alpha} = \frac{3}{4} C_{6563} EW_{H\alpha + [N II]}, \quad (8)$$

where the factor  $3/4$  converts the  $H\alpha + [N II]$  equivalent width to that of  $H\alpha$  (Kennicutt 1992). In the case of high redshift galaxies ( $z > 0.3$ ), where  $H\alpha$  is redshifted outside the observable window, we use  $[O II] 3727$  emission line to measure the star formation, relating the  $[O II] 3727$  equivalent width to that of  $H\alpha$  via

$$EW_{[O II]} = 0.4 \times EW_{H\alpha + [N II]}, \quad (9)$$

derived by Kennicutt (1992) for a sample of local galaxies spanning a wide range of types.

The  $L_{H\alpha}$  versus  $P_{1.4}$  relation is shown in Figure 14.

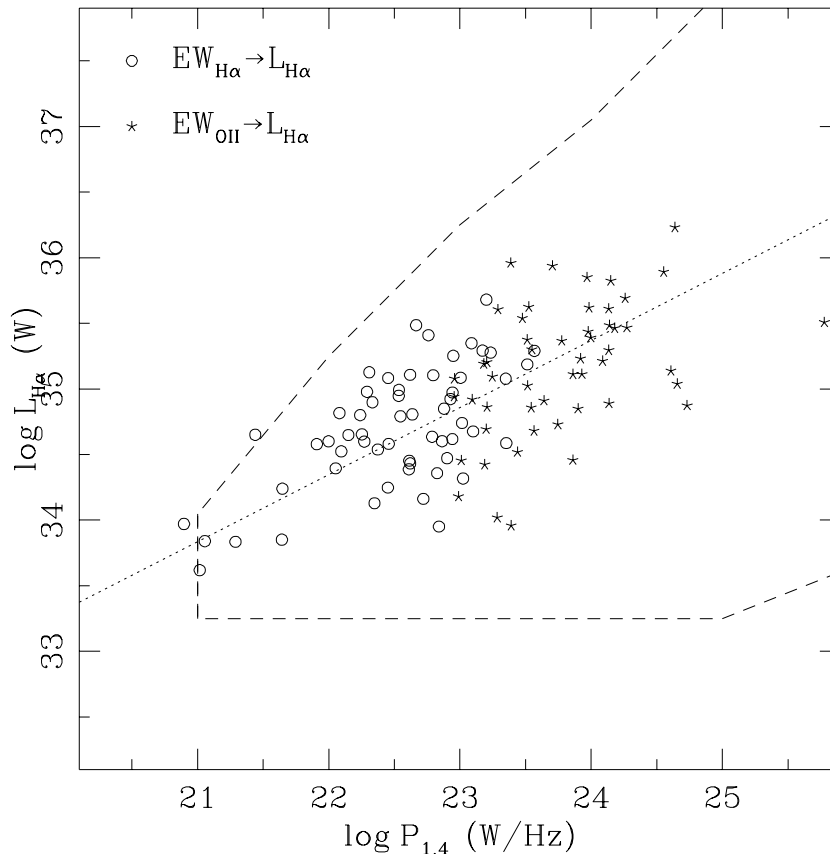


**Figure 14.** Relation between radio power and H $\alpha$  luminosity. Open circles (o) correspond to radio galaxies with  $z < 0.3$ , where H $\alpha$  lies within the observable window. Asterisks (\*) correspond to radio galaxies at higher redshifts, where H $\alpha$  is redshifted outside the optical window. For these objects we employ [O II] 3727 as a proxy to H $\alpha$ . The dotted line represents the best fit to the data  $L_{\text{H}\alpha} \propto P_{1.4}^{-0.6}$ . The dashed line delimits the region of the parameter space affected by the selection effects, as described in the text.

To remove any artificial trend in this relation due to incompleteness, we only consider galaxies with optical magnitudes brighter than  $m_R = 21.5$  mag and radio fluxes brighter than 0.4 mJy, in the case of the PDF, or brighter than 0.2 mJy in the case of PDFS. Assuming a linear relation between  $P_{1.4}$  and  $L_{\text{H}\alpha}$  we find  $L_{\text{H}\alpha} = 10^{12} P_{1.4}$ , in excellent agreement with that independently found by Benn *et al.* (1993). However, the best fit to the data is a power law of the form  $L_{\text{H}\alpha} \propto P_{1.4}^{-0.6}$  (dotted line in Figure 14). This relation also holds if the  $z < 0.3$  and the  $z > 0.3$  sources are treated separately.

However, Figure 14 is not free of selection effects. Firstly, the radio survey is peak flux density limited and complete to  $\approx 0.4$  mJy. Secondly, the spectroscopic observations are carried out only for the optically identified galaxies in the radio sample, introducing a bias against optically faint sources.

To confirm the reality of the trend seen in Figure 14, we will assume that  $L_{\text{H}\alpha}$  and  $P_{1.4}$  are uncorrelated and we will investigate if the selection effects introduce any artificial relation between these two quantities. We adopt a limiting optical magnitude  $m_R = 21.5$  mag, corresponding to the faintest object for which a redshift has been estimated and a radio

flux density limit of 0.4 mJy. To calculate the optical K-corrections we adopt the Sab/Sbc galaxy model generated by the population synthesis code of Bruzual and Charlot (1993; Appendix C). This will also be used to calculate  $L_{\text{H}\alpha}$  via (Kennicutt 1992)

$$SFR = \frac{L_{\text{H}\alpha}}{8.9 \times 10^{34} W} M_{\odot} \text{ yr}^{-1}, \quad (10)$$

where the star formation rate (SFR) is given by the model. An average correction of 1.0 mag, to allow for dust extinction (Kennicutt 1992), is also applied to this equation.

The apparent magnitude  $m_R$  and flux density  $S_{1.4}$ , corresponding to a given set of values  $M_R$  ( $M_R < -20.0$  mag) and  $P_{1.4}$  ( $P_{1.4} > 20.0 \text{ W Hz}^{-1}$ ) respectively, are calculated, for redshifts in the range  $0 < z < 1.5$  (corresponding to the  $z$  range of the sources in our sample). If  $m_R$  and  $S_{1.4}$  lie within the optical and radio completeness limits respectively, the values of  $M_R$  and  $P_{1.4}$  are registered. Following this procedure, we define the bias free region in Figure 14, demarcated by the dashed lines. It is obvious that the sample selection is not significantly affecting our results.

Furthermore, the 2dF fibre size might also introduce a bias into our sample. If the H $\alpha$  emitting region is large,

we may have underestimated the  $H\alpha$  equivalent width and hence the  $H\alpha$  luminosity, for nearby extended galaxies. That could induce a false correlation in Figure 14 (Leech *et al.* 1988). However, most of the sources in our sample, lie at redshifts  $> 0.1$  and therefore this effect is expected to be small.

We conclude that the strong correlation between radio power and  $H\alpha$  luminosity in Figure 14 is real. This is interpreted as the result of the tight correlation between far-infrared and radio power (Condon 1992) and  $H\alpha$  and far-infrared luminosities (Leech *et al.* 1988). Therefore, the radio power can also be used as a probe of the star-formation activity in starburst galaxies. Additionally, the insensitivity of radio luminosities to dust extinction compared to  $H\alpha$  provides further advantage in using this to study the star-formation.

## 5 CONCLUSIONS

The 1.4 GHz Phoenix radio survey has provided a homogeneous sample of sources which we have used to study the nature of the faint radio population. Our conclusions are summarised below:

(i) many of the optical counterparts of sub-mJy radio sources have  $V-R$  colours and spectroscopic properties, similar to those of star-forming galaxies. However, radio sources with absorption line spectra, similar to those of ellipticals, are also found at sub-mJy levels.

(ii) the average visual extinction of the  $z < 0.3$  star-forming galaxies that host faint radio sources appears to be similar to that of normal galaxies (Kennicutt 1992).

(iii) the  $V-R$  and  $R-K$  colours of the optical counterparts of faint radio galaxies are generally consistent with moderate amounts of extinction, with a small fraction of galaxies having evidence of higher extinction.

(iv) simple population synthesis models with dust reddening can reproduce the observed range of radio-to-optical luminosity ratios and the rest-frame  $V-R$  colours of star-forming radio galaxies.

(v) the radio power of star-forming galaxies correlates with  $H\alpha$  luminosity, indicating that the former probes the active star-formation in these objects.

## 6 ACKNOWLEDGEMENTS

We wish to thank an anonymous referee for several constructive comments. AG is supported by a scholarship from the State Scholarships Foundation of Greece (S.S.F.). The work of LC and AH is supported by the Australian Research Council and the Science Foundation for Physics within the University of Sydney.

## REFERENCES

Allington-Smith J. R., 1982 MNRAS, 201, 331  
 Bahcall J. N., Soneira R. M., 1980, ApJS, 44, 73  
 Baldwin J. A., Phillips M. M. & Terlevich R., 1981, PASP, 93, 5  
 Benn C. R., Rowan-Robinson M., McMahon R. G.,  
 Broadhurst T. J., & Lawrence A., 1993, MNRAS, 263, 98  
 Brocklehurst M., 1971, MNRAS, 153, 471

Bruzual A. G., Charlot S., 1993, ApJ, 405, 538  
 Carter B. S., Meadows V. S., 1995, MNRAS, 276, 734  
 Chambers K. C., Charlot S., 1990, ApJ, 348L, 1  
 Coleman P. H., Condon J. J., 1985, AJ, 90, 143  
 Condon J. J., 1989, ApJ, 338, 13  
 Condon J. J., 1992, ARA&A, 30, 575  
 Dahari O., De Robertis M. M., 1988, ApJ, 331, 727  
 Danese L., De Zotti G., Franceschini A., 1985, A&A, 143, 277  
 Danese L., De Zotti G., Franceschini A., Toffolatti L., 1987, ApJ, 318, L15  
 Dunlop J. S., Peacock J. A., 1990, 247, 19  
 Downes A. J. B., Peacock J. A., Savage A., Carrie D. R., 1986, MNRAS, 218, 31  
 Elston R., Cornell M. E., Lebofsky M. J., 1985, ApJ, 296, 106  
 Fomalont E. B., Kellermann K. I., Richards E. A., Windhorst R. A., Partridge R. B., 1997, ApJ, 475, L5  
 Griensmith D., 1980, AJ, 85, 1295  
 Gruppioni C., Mignoli M., Zamorani G., 1998, astro-ph/9811309  
 Guzman R., Gallego J., Koo D. C., Phillips A. C., Lowenthal J. D., Faber S. M., Illingworth G. D., Vogt N. P., 1997, ApJ, 489, 559  
 Hammer F., Crampton D., Lilly S. J., Le Fevre O., Kenet T., 1995, MNRAS, 276, 1085  
 Hamuy M., Suntzeff N. B., Heathcote S. R., Walker A. R., Gigoux P., Phillips M. M., 1994, PASP, 106, 566  
 Hopkins A., Mobasher B., Cram L., Rowan-Robinson M., 1998, MNRAS, 296, 839  
 Hopkins A., 1998a, Ph.D. thesis, University of Sydney  
 Hudon J. D., Lilly J. S., 1996, ApJ, 469, 519  
 Jarvis J. F., Tyson J. A., 1981, AJ, 86, 476  
 Kennicutt R. C., Keel W. C., Blaha C. A., 1989, ApJ, 337, 761  
 Kennicutt R. C., 1992, ApJ, 388, 310,  
 Klein U., 1982, A&A, 116, 175  
 Kron R. G., Koo D. C., Windhorst R. A., 1985, A&A, 146, 38  
 Landolt A. U., 1992, AJ, 104, 372  
 Ledlow M. J., Owen F. N., 1996, AJ, 112, 9  
 Leech K. J., Lawrence A., Rowan-Robinson M., Walker D., Penston M. V., 1988, MNRAS, 231, 977  
 Lilly S. J., 1989, ApJ, 340, 77  
 McCarthy J. P., 1993a, ARA&A, 31, 639  
 Metcalfe N., Shanks T., Fong R., Jones L. R., 1991, MNRAS, 249, 498  
 Metcalfe N., Shanks T., Fong R., Roche N., 1995, MNRAS, 274, 257  
 Oort M. J. A., Katgert P., Steeman F. W. M., Windhorst R. A., 1987, A&A, 179, 41  
 Pozzetti L., Bruzual G. & Zamorani G., 1996, MNRAS, 281, 953,  
 Radford S. J. E., Downes D., Solomon P. M., 1991, ApJ, 368L, 15  
 Rixon G. T., Wall J. V., Benn C. R., 1991, MNRAS, 251, 243  
 Rola C. S., Terlevich E., Terlevich R. J., 1997, MNRAS, 289, 419  
 Rowan-Robinson M., Benn C. R., Lawrence A., McMahon R. G., & Broadhurst T. J., 1993, MNRAS, 263, 123  
 Sandage A., Visvanathan N., 1978, ApJ, 223, 707  
 Savage B. D. & Mathis J. S., 1979, ARA&A, 17, 73  
 Schroeder A., 1996, PASP, 108, 829  
 Scoville N. Z., Sanders D. B., Sargent A. I., Soifer B. T., Inney C. G., 1989, ApJ, 345L, 25  
 Scoville N. Z., Sargent A. I., Sanders D. B., Claussen M. J., Masson C. R., Lo K. Y., Phillips T. G., 1986, ApJ, 303, 416  
 Scoville N. Z., Sargent A. I., Sanders D. B., Soifer B. T., 1991, ApJ, 366L, 5  
 Thuan X. T., Windhorst R. A., Puschell J. J., Isaacman B. R., Owen F. N., 1984, ApJ, 285, 515  
 Thuan X. T., Condon J. J., 1987, ApJ, 322, L9  
 Thuan X. T., Patterson R. J., Condon J. J., Mitchell K. J., 1992, AJ, 104, 133

Tresse L., Rola C., Hammer F., Stasinska G., Le Fevre O., Lilly S. J., Crampton D., 1996, MNRAS, 281, 847  
 Veilleux S., Osterbrock D. E., 1978, ApJS, 63, 295  
 Veilleux S., Kim D. C., Sanders D. B., Mazzarella J., M., Soifer B. T., 1995, ApJS, 98, 171  
 Wainscoat R. J., Cowie L. L., 1992, AJ, 103, 322  
 Windhorst R. A., Miley K. G., Owen F. N., Kron R. G., David C. K., 1985, ApJ 289, 494  
 Windhorst R. A., Fomalont E. B., Partridge R. B., Lowenthal J. D., 1993, ApJ, 405, 498  
 Windhorst R. A., Fomalont E. B., Kellerman K. I., Partridge R. B., Richards E., Franklin B. E., Pascarella S. M., Griffiths R. E., 1995, Nature, 375, 471  
 Yoshii Y., Takahara F., 1988, ApJ, 326, 1

## APPENDIX A: STAR-GALAXY SEPARATION

The galaxy number counts provide a useful consistency check between our optical catalogue and other surveys. However, although the FOCAS number counts at faint magnitudes are dominated by galaxies, at bright magnitudes ( $m_R < 19.0$ , Hudon & Lilly 1996), the stellar component makes a significant contribution. To correct for this stellar contamination we adopt the following procedure. We considered a size parameter, defined as the difference between the ‘core’,  $m_{core}^R$ , and ‘total’,  $m_{total}^R$ , magnitude of sources. The former corresponds to the intensity within the  $3 \times 3$  inner pixels of an object and the latter is the integrated luminosity within an aperture defined by adding rings around the object until the detection area is exceeded by a factor of 2. This difference is then plotted against  $m_{total}^R$  (Fig. A1). Since the size parameter is sensitive to the seeing, the data taken in different conditions, should be treated separately. Consequently, we grouped the images of a given night according to the seeing conditions at the time of the observation and performed the star-galaxy separation for each group individually. This is demonstrated in Figure A1 where the size parameter is plotted against the ‘total’ magnitude for frames with similar seeing conditions, with the stellar sequence demarcated with a solid lined rectangular box. The distribution of stars and galaxies in this figure overlaps at magnitudes fainter than  $m_R = 20.0$  mag. Beyond that magnitude limit no attempt is made to further eliminate stars from the sample, since compact galaxies could be mistakenly removed. Furthermore, the number of stars relative to galaxies becomes increasingly smaller beyond this magnitude.

The galaxy number counts are shown in Figure A2 along with the compilation of Metcalfe *et al.* (1991). For  $m_R < 22.5$  mag our counts seem to be in good agreement with the recent determinations. At fainter magnitudes the sample is affected by incompleteness. Additionally, the star counts in Figure A2 (small circles) are also in good agreement with the predictions of the model of Bahcall & Soneira (1980).

## APPENDIX B: $H\beta$ ABSORPTION

To estimate the average  $H\beta$  absorption for the sample of  $z < 0.3$  radio sources (where  $H\alpha$  lies within the observable window), we consider the relation between the  $H\beta$  and  $H\alpha + [NII]$  equivalent widths for star-forming galaxies and Seyfert 2 type objects, presented in Figure B1. Additionally, radio galaxies with absorption line spectra (for which

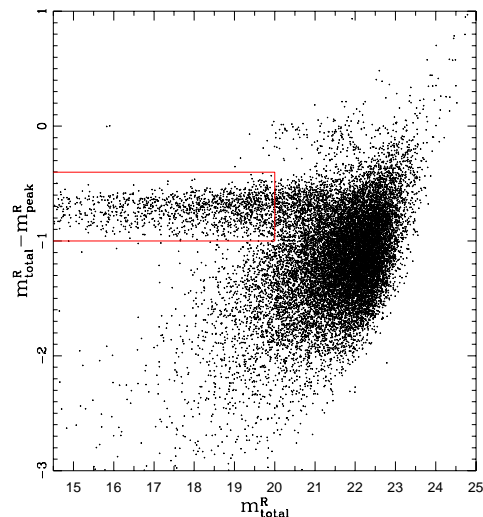


**Figure A1.** Star-galaxy separation diagram for a subset of the  $R$ -band observations performed in similar seeing conditions. The stellar sequence is demarcated by a box.

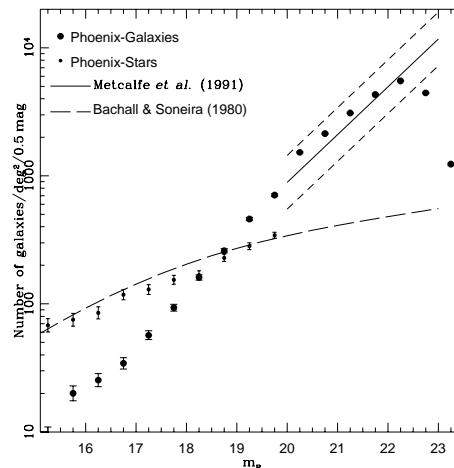


**Figure A2.**  $R$ -band galaxy counts (big circles) of the Phoenix field. The continuous line is the best fit to the galaxy source counts in the range  $20 < m_R < 23$  by Metcalfe *et al.* (1991). The dashed lines are the  $1\sigma$  envelope lines. Also shown are the star counts (small circles) from the present study, along with the predictions of the model of Bahcall & Soneira (1980).

$EW_{H\beta} \leq 0$ ) and only  $H\alpha$  emission line, classified star-forming galaxies in section 4.1, are also plotted in Figure B1. The best fit to the data, shown with the continuous line in that Figure, follows the relation

$$EW_{H\beta} = EW_{H\alpha + [NII]} / (9.1 \pm 0.4) - (1.7 \pm 0.3). \quad (B1)$$

The coefficients in equation (B1) imply a mean  $H\beta$  absorption of  $-1.7 \pm 0.3 \text{ \AA}$ . Kennicutt (1992), following a similar

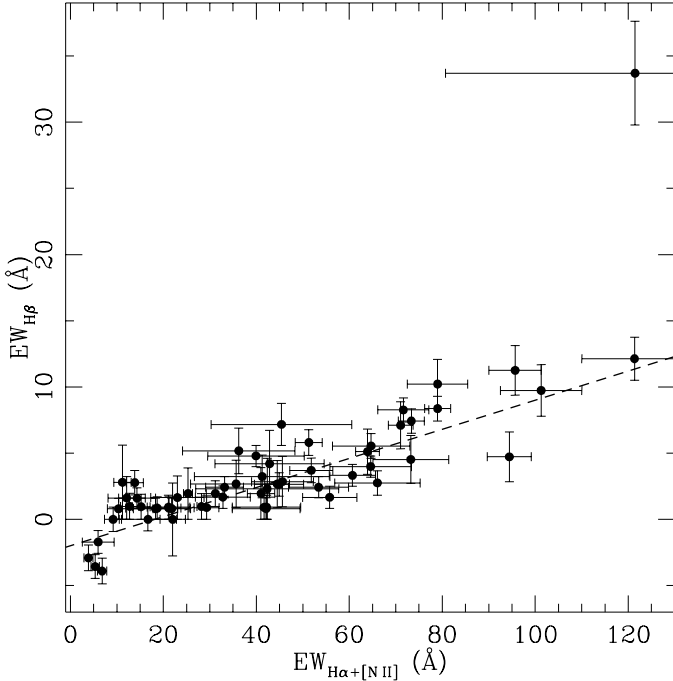


**Figure B1.** Relation between the  $H\beta$  and  $H\alpha+[N II]$  equivalent widths. The dashed line is the best fit to the data, given by the relation  $EW_{H\beta} = EW_{H\alpha+[N II]} / (9.1 \pm 0.4) - (1.7 \pm 0.3)$ .

procedure, found an average stellar  $H\beta$  absorption of  $\approx -5 \text{ \AA}$  for normal galaxies. However, a value of  $-2 \text{ \AA}$  is usually used in the literature for H II regions (Tresse *et al.* 1996), in good agreement with our result.

### APPENDIX C: POPULATION SYNTHESIS MODELS

In this study we adopt the galaxy models developed by Pozzetti, Bruzual & Zamorani (1996) that make use of the population synthesis code of Bruzual & Charlot (1993) to generate evolutionary models for ellipticals (E/S0), early (Sab/Sbc) and late (Scd/Sdm) type spirals and very blue galaxies (vB), meant to reproduce the starburst population present at each redshift.

Assuming  $H_o = 50 \text{ km}^{-1} \text{ s}^{-1} \text{ Mpc}^{-1}$ ,  $q_o = 0.5$  and a formation redshift of  $z_f = 10$ , corresponding to an age of 12.7 Gyr, the adopted parameters for the different galaxy types, are listed in Table C1. The local properties of E/S0 and Sab/Sbc galaxies are best represented by an exponentially decaying Star Formation Rate (SFR), of the form  $\psi(t) \propto \tau^{-1} \exp(-t/\tau)$ , where  $\tau$  is the e-folding time. A value of  $\tau=1$  and 8 Gyr was adopted for the E/S0 and Sab/Sbc galaxies respectively. Late type spirals and starbursts are best represented by a constant SFR and different ages.

Model SED	SFR	IMF	Age (Gyr)
E/S0	$\tau_1$	Scalo	12.7
Sab/Sbc	$\tau_8$	Scalo	12.7
Sbc/Scd	constant	Salpeter	12.7
vB	constant	Salpeter	0.1

**Table C1.** The Star-Formation Rate (SFR), Initial Mass Function (IMF) and present day galaxy age adopted to construct the Spectral Energy Distributions (SEDs) of different galaxy types.